# **Inorganic Chemistry**

pubs.acs.org/IC Article

## Influence of Rare-Earth Ion Radius on Metal—Metal Charge Transfer in Trinuclear Mixed-Valent Complexes

Cole Carter, Yosi Kratish,\* and Tobin J. Marks\*



Cite This: Inorg. Chem. 2023, 62, 4799-4813



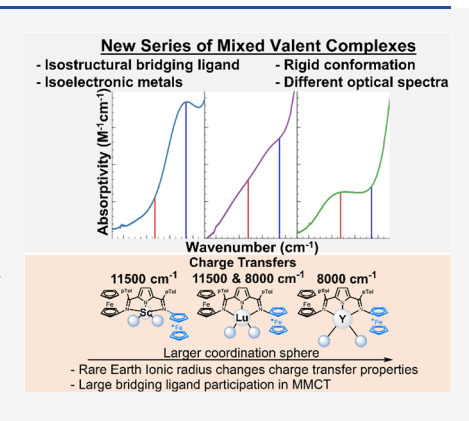
**ACCESS** 

Metrics & More

Article Recommendations

S Supporting Information

**ABSTRACT:** We report the synthesis and characterization of a highly conjugated bisferrocenyl pyrrolediimine ligand, Fc<sub>2</sub>PyrDIH (1), and its trinuclear complexes with rare earth ions—(Fc<sub>2</sub>PyrDI)M(N(TMS)<sub>2</sub>)<sub>2</sub> (2-M, M = Sc, Y, Lu, La). Crystal structures, nuclear magnetic resonance (NMR) spectra, and ultraviolet/visible/near-infrared (UV/vis–NIR) data are presented. The latter are in good agreement with DFT calculations, illuminating the impact of the rare earth ionic radius on NIR charge transfer excitations. For [2-Sc]<sup>+</sup>, the charge transfer is at 11,500 cm<sup>-1</sup>, while for [2-Y]<sup>+</sup>, only a d—d transition at 8000 cm<sup>-1</sup> is observed. Lu has an ionic radius in between Sc and Y, and the [2-Lu]<sup>+</sup> complex exhibits both transitions. From time-dependent density functional theory (TDDFT) analysis, we assign the 11,500 cm<sup>-1</sup> transition as a mixture of metal-to-ligand charge transfer (MLCT) and metal-to-metal charge transfer (MMCT), rather than pure metal-to-metal CT because it has significant ligand character. Typically, the ferrocenes moieties have high rotational freedom in bisferrocenyl mixed valent complexes. However, in the present (Fc<sub>2</sub>PyrDI)M(N(TMS)<sub>2</sub>)<sub>2</sub>



complexes, ligand-ligand repulsions lock the rotational freedom so that rare-earth ionic radius-dependent geometric differences increasingly influence orbital overlap as the ionic radius falls. The Marcus-Hush coupling constant  $H_{AB}$  trends as  $[2-Sc]^+ > [2-Lu]^+ > [2-Y]^+$ .

#### ■ INTRODUCTION

When multiple transition metal ions are connected by a delocalized bridging ligand, the conjugation can allow the dorbitals on the metal ions to electronically couple to each other. This coupling enables electron transfer between metal centers and delocalization of d-electrons across the bridge. While the properties and physical underpinnings of such electronic coupling between redox-active metal centers in mixed valent systems have been well studied, 1-3 there are still challenges in understanding structure-property relationships in complex molecules. Generally, mixed-valent systems are studied by permutating a library of conjugated bridging ligands and observing the effects of substitution to infer the variables influencing the metal-to-metal charge transfer (MMCT) that arises from electronic coupling.<sup>4</sup> However, it is often difficult to predict which bridging ligands will lead to strong MMCTs, given that electronic coupling can be very sensitive to variables that are difficult to finely tune and deconvolute, such as bond angles, torsions, energetic separation between orbitals, solvation, etc. Furthermore, in solution, thermal motion can result in an ensemble of geometries that may be averaged on the spectroscopic timescale.<sup>4</sup> Because any substitution often changes both molecular and electronic structure, it can be difficult to isolate variables for analysis. One such challenging variable is the effect of extended nuclearity in a mixed valent system. Metallation often has dramatic impacts on both the geometry and electronics of the ligand, with the exact effects

depending on the identity of the metal. To this end, it would be desirable to design bridging ligands that are both rigid and can accommodate multiple metal types in a symmetric geometry to decrease the number of free variables when analyzing MMCT properties.

Fortunately, the field of noninnocent ligands has established several families of conjugated ligands that display extensive delocalization between metals and ligands, 5-7 suggesting them as good candidates as bridging ligands. Such metal-ligand delocalization can be considered a form of metal—organic mixed valency, harnessing proper orbital overlaps and orbital energies for delocalization across the complex. Using such ligands as a starting point provides well-studied electronic structures and modular syntheses for exploring traditionally challenging to study elements of electronic coupling. For example, studying the effect of increasing nuclearity in an already electronically coupled mixed valent system is a challenging synthetic problem (e.g., installing multiple binding sites that can be metallated in a controlled way) for which

Received: November 10, 2022 Published: March 15, 2023





**Inorganic Chemistry** Article pubs.acs.org/IC

there is no obvious general strategy. Additionally, investigations of the direct participation of the bridging ligand in electron transfer mechanisms where the charge transfer is a blend of MLCT (or LMCT) and MMCT require bridging ligands with significant electronic coupling between the metal and ligand in addition to coupling between metals, which is afforded by noninnocent ligands. From the noninnocent ligand literature, we know that metal binding and delocalization of frontier orbitals between metal and ligand impart emergent properties to the complex.<sup>8–10</sup> As such, one reasonably expects that by converting a noninnocent ligand into a mixed valent system by replacing aryl groups with redox-active groups such as ferrocenyls, it should be possible to generate a mixed valent compound that can bind to an additional metal. In this design, we can modify the geometry and electronics of the bridging organic linker between ferrocenes by permutating the additional third metal.

In a recent study, we reported that the addition of a metal ion to a bis-ferrocenyl pyridinediimine ligand switched it from a Class 1 to a Class 2 mixed valent system (Figure 1A).1

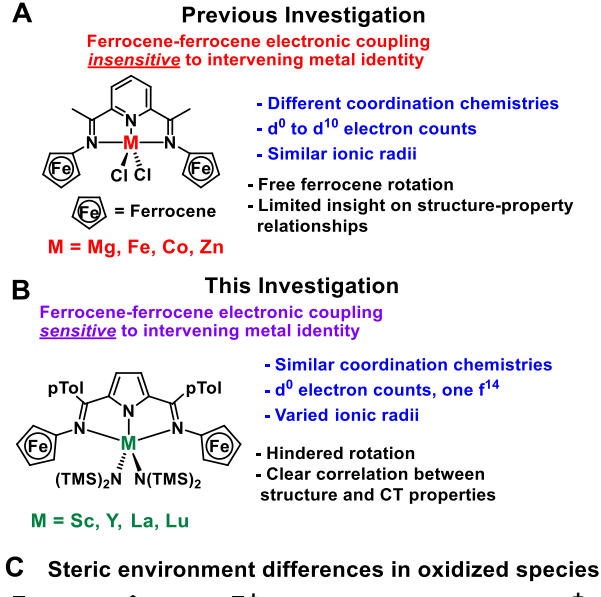


Figure 1. Comparison of (A) TM-pyridine and (B) RE-pyrrolate complexes and their mixed valent properties. (C) Different steric environments afforded by the RE-pyrrolate complexes.

Interestingly, the additional metal ion did not participate directly in the electronic coupling itself nor did metal ions of different coordination chemistries (Mg, Fe, Co, and Zn) impart significantly different coupling properties. This raised questions about whether structural influences from metalation are relevant to the emergent behavior of electronic coupling even if varying coordination chemistries were not. Metallation of polydentate delocalized ligands has many effects on the

ligand itself, such as electron withdrawal/donation from Lewis acidic/basic d-orbitals and rigidification/templating of the ligand around the metal ion. Isolating such variables is vital to understanding how the interaction between a bis-ferrocenyl ligand and an extra metal center affects the interaction between ferrocenes. However, when working with transition metal ions, it is challenging to isolate the geometric and electronic effects that the metal has on the surrounding ligands. Transition metal ions have different levels of covalency, preferred coordination geometry, and acidity/basicity that are interdependent and difficult to deconvolute. In contrast, rare earth ions (defined by IUPAC as the lanthanides as well scandium and yttrium)<sup>12</sup> are generally thought to display very similar coordination chemistries, 13 but differ primarily in the ion size, and thus charge density. These ionic radius differences  $^{14}$  (r = 88.5, 100,and 104 pm for Sc, Lu, and Y, respectively) can change the polarization across the ligand due to different charge densities and alter bond and torsion angles as a result of different-sized coordination spheres (Figure 1B). 15-17 Recognizing this opportunity to isolate the influence of metal ionic radius from intrinsic coordination chemistry, here we synthesize and characterize a series of d<sup>0</sup> rare earth complexes coordinated by an anionic bis-ferrocene pyrrolediiminato ligand (Figure 1B,C). In doing so, we probe the effects of the metal ion size on the electronic structures of the mixed valent state in these complexes and, consequently, its role in modulating the charge transfer between ferrocene moieties.

#### **EXPERIMENTAL SECTION**

General Considerations. All procedures for air- and moisturesensitive compounds were carried out with rigorous exclusion 18 of O2 and moisture in flame or oven-dried Schlenk-type glassware interfaced to a dual-manifold Schlenk line or Ar-fed high-vacuum (<10<sup>-6</sup>-10<sup>-7</sup> Torr) line using an oil diffusion pump, or in an Ar-filled Mbraun glovebox with a high capacity recirculator (<0.5 ppm O<sub>2</sub>). Argon for high-vacuum lines (Airgas, UHP grade) was purified by passage through MnO/vermiculite and Davison 4 Å molecular sieve columns. 19 Where relevant, solvents are designated as from a Pure Process Technology solvent purification system (SPS) or dried more rigorously. More rigorously dried solvents were stirred over potassium metal overnight, after which a few large crystals of benzophenone were added. After degassing through freeze-pump-thaw cycles, the Teflon-sealed flask (still containing potassium and under vacuum) was stirred overnight at 70 °C (or 40 °C for pentane). For pentane and heptane, a small amount of tetraglyme or 18-crown-6 was added to improve the solubility of the ketyl radical. NMR solvents were purchased from Cambridge Isotope Laboratories or Sigma Aldrich (>99 atom % D). Solvents used for NMR characterization of pyrrole and ferrocene intermediates were used as received, while C<sub>6</sub>D<sub>6</sub> for characterization of rare earth complexes was dried over potassium metal as described above. Iodoferrocene, 20 aminoferrocene, 21 metal tris(bistrimethylsilyl) amides (metal = Sc, Y, Lu, La),<sup>22</sup> and 2,5ditolylacetylpyrrole<sup>23</sup> were synthesized according to literature procedures.

Physical and Analytical Measurements. Solution <sup>1</sup>H and <sup>13</sup>C NMR spectra were recorded on either a 400 MHz Bruker Avance III Nanobay system with a BBFO Smart probe or a 500 MHz Bruker Avance III HD system equipped with a BBO Prodigy probe. Chemical shifts for <sup>1</sup>H and <sup>13</sup>C spectra were referenced using residual solvent resonances and are reported relative to tetramethylsilane (TMS). Ultraviolet/visible/near-infrared (UV/vis-NIR) measurements were taken on an Agilent Cary 5000 double beam spectrophotometer, using a 2 mm quartz cuvette from Spectrocell (transparent to 3000 nm) modified with a Teflon-sealed valve and ground glass joint. Elemental analyses were performed in an air-free glovebox by Midwest Microlab, Indianapolis, Indiana, for % C, N, H.

**Computational Methods.** All quantum chemical calculations were performed using Orca 5.0.<sup>24</sup> Geometry optimizations of all complexes were carried out at the B3LYP<sup>25–28</sup>/ZORA-def2-TZVP level of theory, with the ZORA-def2-SVP basis set on carbon and hydrogen using ZORA relativistic and D3 dispersion corrections. Frequency and time-dependent density functional theory (TDDFT) calculations were performed at the same level of theory to validate energy minima. To compute the UV/vis–NIR spectra, solvent effects from dimethoxyethane were calculated through the Continuous Polarizable Continuum Model (CPCM)<sup>29</sup> using a refractive index and a dielectric constant of 1.379 and 7.2, respectively.<sup>30,31</sup>

**Crystallography.** Single crystals suitable for diffraction were mounted in Paratone oil and transferred to the cold nitrogen gas stream of a Rigaku Synergy system with a MoK $\alpha$  microsource. The crystal was maintained at 100.0 K during data collection. The structures were solved using Olex2 1.5<sup>32</sup> with the XT structure solution program<sup>33</sup> and refined using the ShelXL refinement package<sup>34</sup> with full-matrix least-square procedures.

Spectroelectrochemistry. SpecEchem was performed in an Inert Atmosphere glovebox using a 1.7 mm Pine Research electrolysis cuvette with a platinum honeycomb electrode chip with a nonaqueous Ag/AgNO<sub>3</sub> reference electrode from Pine Research. The 300–1050 nm spectra were collected using a BWTek BRC741E-02 diode array detector connected via fiber optic cables to the sample inside the glovebox. Electrolysis was carried out with a WaveNow potentiostat using a linear sweep at a rate of 5 mV/s starting at 0 V vs reference. NIR data past 1050 nm was collected by baselining a UV-vis-NIR instrument with a solvent blank. Then, the sample spectrum was recorded before and after one equivalent of Magic Blue (tris(parabromophenyl) aminium hexachloroantimonate)<sup>35</sup> was added to the sample cuvette (2 mm NIR cuvette from the spectrocell, described above).

Syntheses. Fc<sub>2</sub>PyrDIH (1). Diphenylacetic acid (500 mg, 2.4 mmol, 0.4 eq), 2,5-ditolylacetal pyrrole (2.5 g, 8.2 mmol, 1 eq), and FcNH<sub>2</sub> (4.2 g, 20 mmol, 2.5 eq) were added to a dry Schlenk flask under an inert atmosphere. A dry Soxhlet apparatus was attached, and the thimble was charged with activated molecular sieves similar to that described by Stoltz.<sup>36</sup> Then, 25 mL of toluene from an SPS was added by syringe, and the reaction was allowed to reflux briskly for four days, over which time the solution turned dark red. The reaction mixture was then cooled to room temperature, loaded onto a deactivated (5-10% m/m H<sub>2</sub>O/alumina) basic alumina column, and eluted with a 15-40% EtOAc/hexanes gradient. The red solid product was further purified by crystallization from a THF/H2O layered mixture. The red crystalline product was partially dissolved in heptane, and the solvent was evaporated under vacuum to aid in removing THF and water. This procedure was repeated three times. Subsequent drying under vacuum overnight afforded a bench-stable red solid. Isolated yield: 1.1 g (45%). If desired, the intermediate monoimine can be recovered from the column as a purple solid and recycled for further imine condensations. Crystals suitable for X-ray crystallography were obtained in the column fractions following chromatography (approximately 20% EtOAc/hexanes). <sup>1</sup>H NMR (C<sub>6</sub>D<sub>6</sub>, 500 MHz): 11.03 (s, 1H, N-H), 7.19 (m, 4H, ortho-tol), 6.94 (m, 4H, meta-tol), 6.23 (s, 2H, pyr-3,4), 4.12 (s, 10H,  $C_5H_5$ ), 4.07 (t, J = 1.8 Hz, 4H, Cp- $\beta$ ), 3.87 (t, J = 1.8 Hz, Cp- $\gamma$ ), 2.08 (s, 6H, tol-CH<sub>3</sub>). <sup>13</sup>C NMR (C<sub>6</sub>D<sub>6</sub>, 126 MHz): 157.3(C=N), 138.6 (pyr-2,5), 137.4 (para-tol), 135.2 (ipso-tol), 129.4 (meta-tol), 128.6 (ortho-tol), 115.4 (pyr-3,4), 103.1 (Cp- $\alpha$ ), 70.0 (Cp,  $C_5H_5$ ), 67.2 (Cp- $\beta$ ), 66.6 (Cp- $\gamma$ ), 21.3 (tol-CH<sub>3</sub>). Anal. calcd for Fc<sub>2</sub>PyrDI, formula C<sub>29</sub>H<sub>27</sub>N<sub>3</sub>Fe<sub>2</sub>: C, 65.81; H, 5.14; N, 7.94. Found: C, 65.66; H, 4.99; N, 7.87.

(Fc<sub>2</sub>PyrDl)Sc(N(TMS)<sub>2</sub>)<sub>2</sub> (**2-Sc**). Fc<sub>2</sub>PyrDlH (100 mg, 0.15 mmol, 1 eq) and Sc(N(TMS)<sub>2</sub>)<sub>3</sub> (79 mg, 0.15 mmol, 1 eq) were added to a Teflon-sealed reaction tube inside a glovebox. Then, 50 mL of toluene was vacuum-transferred directly into the reaction tube from purple K/benzophenone ketyl solution. This evacuated tube was heated to 70 °C for 48 h, over which time it changed color from red to brown/green. The vessel containing the crude reaction product was taken back into the glovebox and the solution was transferred to a flip-frit with o-ring sealed ball and socket joints. The vessel was placed under

high vacuum (1  $\times$  10<sup>-6</sup> Torr), and toluene was evaporated. Next, heptane was vacuum-transferred in (from purple K/benzophenone ketyl). Differential pressure for filtration was generated by cooling the receiving flask. After filtration, heptane was recondensed into the solid flask with dry ice/acetone and extracted again. This process was repeated until the heptane extract was no longer brown and was a faint green color. Toluene was then added back to the solids and slowly evaporated under vacuum. When concentrated to ca. 2 mL, toluene was decanted to leave behind purple microcrystals. A majority of the yield loss occurred during purification due to small differences in solubility between the product and impurities. The product was dried overnight under vacuum to give 64 mg, (41% yield). Crystals suitable for X-ray crystallography were obtained by slow evaporaton of toluene inside of a glovebox at ambient temperature. <sup>1</sup>H NMR (500 MHz,  $C_6D_6$ ):  $\delta = 7.57$  (m, 4H, ortho-tol), 6.98 (m, 4H, meta-tol), 6.23 (d, J = 2.5 Hz, 2H, pyr-3,4), 4.71 (t, J = 1.9 Hz, 4H, Cp- $\beta$ ), 4.04 (t, J = 1.9 Hz, 4H, Cp- $\gamma$ ), 3.81 (s, Cp C<sub>5</sub>H<sub>5</sub>), 2.08 (s, 6H, tol-CH<sub>3</sub>), 0.49 (s, 36H, SiMe<sub>3</sub>). <sup>13</sup>C NMR (126 MHz,  $C_6D_6$ )  $\delta = 168.9$  (C= N), 147. 1 (Pyr-2,5), 128.6 (meta-tol), 128.3 (ortho-tol), 117.6 (Pyr-3,4), 103.0 (Cp- $\alpha$ ), 70.2 (Cp,  $C_5H_5$ ), 69.3 (Cp- $\beta$ ), 66.6 (Cp- $\gamma$ ), 21.3 (tol-CH<sub>3</sub>), 7.1 (SiMe<sub>3</sub>). While there was sufficient purity for investigation (Figure S3), analytical purity was not achieved due to high sample thermal instability, necessitating characterization immediately after synthesis. Elemental analysis is therefore not provided.

(Fc<sub>2</sub>PyrDI)Y(N(TMS)<sub>2</sub>)<sub>2</sub> (2-Y). Fc<sub>2</sub>PyrDIH (100 mg, 0.15 mmol, 1 eq) and  $Y(N(TMS)_2)_3$  (85 mg, 0.15 mmol, 1 eq) were added to a Teflon-sealed reaction tube inside a glovebox. Next, 5 mL of toluene was vacuum-transferred directly into the reaction tube from purple K/ benzophenone ketyl solution. The evacuated tube was then heated to 70 °C for 48 h, over which time it changed color from red to brown/ green. The vessel containing the crude reaction product was taken into a glovebox and transferred to a flipfrit with an o-ring sealed ball and socket joints. The vessel was placed under high vacuum ( $1 \times 10^{-6}$ Torr), and toluene was evaporated. Then, heptane was vacuumtransferred in from purple K/benzophenone ketyl. Differential pressure for filtration was generated by cooling the receiving flask. After filtration, heptane was re-condensed into the solid flask using dry ice/acetone and extracted again. This process was repeated until the heptane extract was no longer brown and was a faint green color. A majority of the yield loss occurred during purification due to small differences in solubility between the product and impurities. Vacuum drying overnight afforded the product as a purple solid (65 mg, 40% yield) <sup>1</sup>H NMR (500 MHz,  $C_6D_6$ ):  $\delta = 7.47$  (m, 4H, ortho-tol), 6.96 (m, 4H, meta-tol), 6.24 (s, 2H, pyr-3,4), 4.62 (t, J = 1.8 Hz, 4H, Cp- $\beta$ ), 4.02 (t, J = 1.8 Hz, 4H, Cp- $\gamma$ ), 3.96 (s, 5H, Cp C<sub>5</sub>H<sub>5</sub>), 2.08 (s, 6H, tol-CH<sub>3</sub>), 0.50 (s, 36H, SiMe<sub>3</sub>). <sup>13</sup>C NMR (126 MHz, C<sub>6</sub>D<sub>6</sub>) 170.1 (C=N), 147.3 (pyr-2,5), 139.6 (para-tol), 128.6 (meta-tol), 128. (ortho-tol), 118.7 (Pyr-3,4), 102.9 (Cp-α), 70.5 (Cp, C<sub>5</sub>H<sub>5</sub>), 68.6  $(Cp-\beta)$ , 66.7  $(Cp-\gamma)$ , 21.3  $(tol-CH_3)$ , 6.8  $(SiMe_3)$ . While there was sufficient purity for investigation (Figure S5), analytical purity was not achieved due to high sample thermal instability necessitating characterization immediately after synthesis. Elemental analysis is therefore not provided.

(Fc<sub>2</sub>PyrDI)Lu(N(TMS)<sub>2</sub>)<sub>2</sub> (**2-Lu**). Fc<sub>2</sub>PyrDIH (100 mg, 0.15 mmol, 1 eq) and Lu(N(TMS)<sub>2</sub>)<sub>3</sub> (98 mg, 0.15 mmol, 1 eq) were added to a Teflon-sealed reaction tube inside a glovebox. Next, 5 mL of toluene was vacuum-transferred directly into the reaction tube from purple K/ benzophenone ketyl solution. This tube was heated to 70 °C for 48 h, over which time it changed color from red to brown/green. Toluene containing the crude reaction product was taken into a glovebox and transferred to a flipfrit with an o-ring-sealed ball and socket joints. The vessel was placed under high vacuum (1  $\times$  10<sup>-6</sup> Torr), and toluene was evaporated to dryness. Dry heptane was vacuumtransferred (off purple K/benzophenone ketyl), and the mixture was filtered. Differential pressure for filtration was generated by cooling the receiving flask. After filtration, heptane was re-condensed into the solid flask using dry ice/acetone and extracted again. This process was repeated until the heptane extract was no longer brown and was a faint green color. Most of the yield loss occurred during purification

Scheme 1. Synthetic Route to Fc<sub>2</sub>PyrDIH (1) Using Previously Reported Conditions To Produce (A) Diacylpyrrole, (B) Amino Ferrocene, and (C) New Conditions To Produce 1 and 1+

due to small differences in solubility between the product and impurities. Vacuum drying overnight affords the product as a purple solid (58 mg, 33% yield). <sup>1</sup>H NMR (500 MHz,  $C_6D_6$ ):  $\delta$  = 7.51 (m, 4H, ortho-tol), 6.96 (m, 4H, meta-tol), 6.23 (s, 2H, pyr-3,4), 4.68 (t, J = 1.9 Hz, 4H, Cp- $\gamma$ ), 4.03 (t, J = 1.9 Hz, 4H, Cp- $\beta$ ), 3.91 (s, Cp  $C_5H_5$ ), 2.08 (s, 6H, tol-C $H_3$ ), 0.50 (s, 36H, SiMe<sub>3</sub>). <sup>13</sup>C NMR (126 MHz,  $C_6D_6$ )  $\delta$  = 169.0 (C=N), 147.0 (pyr-2,5), 139.6 (para-tol), 128.6 (meta-tol) 128.3 (ortho-tol), 117.6 (pyr-3,4), 102.9 (Cp- $\alpha$ ), 70.3(Cp,  $C_5H_5$ ), 69.3 (Cp- $\beta$ ), 66.6 (Cp- $\gamma$ ), 21.5 (tol-C $H_3$ ), 7.1 (SiMe<sub>3</sub>). While there was sufficient purity for investigation (Figure S7), analytical purity was not achieved due to high sample thermal instability necessitating characterization immediately after synthesis. Elemental analysis is thus not provided.

#### RESULTS

Synthesis of Fc<sub>2</sub>PyrDIH (1). While pyridine diimine structures are good ligands for transition metals (Figure 1A), rare earth ions bind only loosely to neutral N-donors and generally require harder anionic O or N donors. For this reason, a pyrrole diimine ligand was targeted for this study (Figure 1B). The precursor 2,5-diacyl pyrroles are generally challenging to prepare. However, McNeece et al.<sup>23</sup> reported a straightforward adaptation of a benzothioloxium protection and pyrrole oxidation protocol, affording 2,5-ditolylacylpyrrole in good yield on a multigram scale. As reported by McNeece et al., the intermediates for diacyl pyrrole were used without purification or characterization between steps. Adding RCOOH (R = pTol) to 2-mercaptophenol in POCl<sub>3</sub> and heating to 110 °C for 10 minutes yielded the benzothioloxium salt, which was isolated by precipitation with HBF4 and ether (Scheme 1A, Step a). Caution: Quenching of large quantities of POCl<sub>3</sub> can lead to large runaway exotherms that can occur rapidly and unexpectedly. Next, the addition of pyrrole to the benzothioloxium salt in acetonitrile at room temperature in the presence of pyridine led to a hot yellow solution which was stirred for 45 min, affording benzothioloxium-protected pyrrole as brown oil after extraction with CHCl<sub>3</sub> and 5% NaOH(aq) wash (Scheme 1A, step b). This oil was suspended in glacial acetic acid, and 30% H<sub>2</sub>O<sub>2</sub> was added, at which point the reaction mixture was heated to 110 °C for 30 min. After cooling, H<sub>2</sub>O and CHCl<sub>3</sub> were added, and the CHCl<sub>3</sub> layer was washed with 10% NaOH<sub>(aq)</sub>. After evaporation, washing the

solid with methanol afforded diacylpyrrole as an off-white solid (30–40% overall yield).<sup>23</sup>

Iodoferrocene was synthesized according to the literature<sup>20</sup> by lithiation of ferrocene with Schlosser base (equimolar <sup>t</sup>BuLi/<sup>t</sup>BuOK) in THF at −78 °C and subsequent lithium− halogen exchange with elemental iodine (1 equiv vs <sup>t</sup>BuLi). An excess (1.5-2 equiv) of 'BulLi/'BuOK can be used to moderately increase yields without dilithiation. Extraction with hexanes and washing with aqueous sat. thiosulfate solution afforded iodoferrocene in good yields (Scheme 1B, step a; typical yields of 60-80%). Iodoferrocene was aminated with 30% NH<sub>4</sub>OH in EtOH at 90 °C for 6 h in a pressure vessel using a Fe<sub>2</sub>O<sub>3</sub>/CuI catalyst system (Scheme 1B, step b).<sup>21</sup> After dilution with ether and an aqueous base wash, the crude amino ferrocene was purified by column chromatography on silica using a 20-70% EtOAc/hexanes gradient to give a polycrystalline orange solid (typical yields: 40-60%). Note: aminoferrocene is moderately air-sensitive and oxidation products can interfere with subsequent chemistry; we recommend storage under an inert atmosphere or purification before use. After repeated use, NH<sub>4</sub>OH degrades viton o-rings, which can lead to reaction failure and/or low yields due to leakage and loss of ammonia and/or introduction of oxygen. The o-ring on the pressure vessel should be inspected and replaced (if necessary) before use. Unfortunately, the subsequent imine condensation (Scheme 1C, step a) suffers from significant thermodynamic and kinetic limitations, as reported by McNeece et al., who condensed diketone at 140 °C in neat cyclohexylamine for 48 h. Since aminoferrocene is a sublimable solid and a more precious substrate, modification of this procedure was required. We find that affixing a Soxhlet apparatus filled with activated (400 °C under diaphragm pump vacuum for 24 h) molecular sieves<sup>36</sup> efficiently desiccates the reaction, enabling high conversions of the diacylpyrrole to roughly 50% diiminopyrrole and 40% monoiminopyrrole. The reaction times appear to be dictated by the water removal rate, which depends on factors such as scale and glassware, so conversions were checked every 24 h by NMR until conversion halted. Monoimine can be isolated for further condensation reactions if desired. An additional modification was replacing the acetic acid catalyst with diphenyl acetic acid to prevent

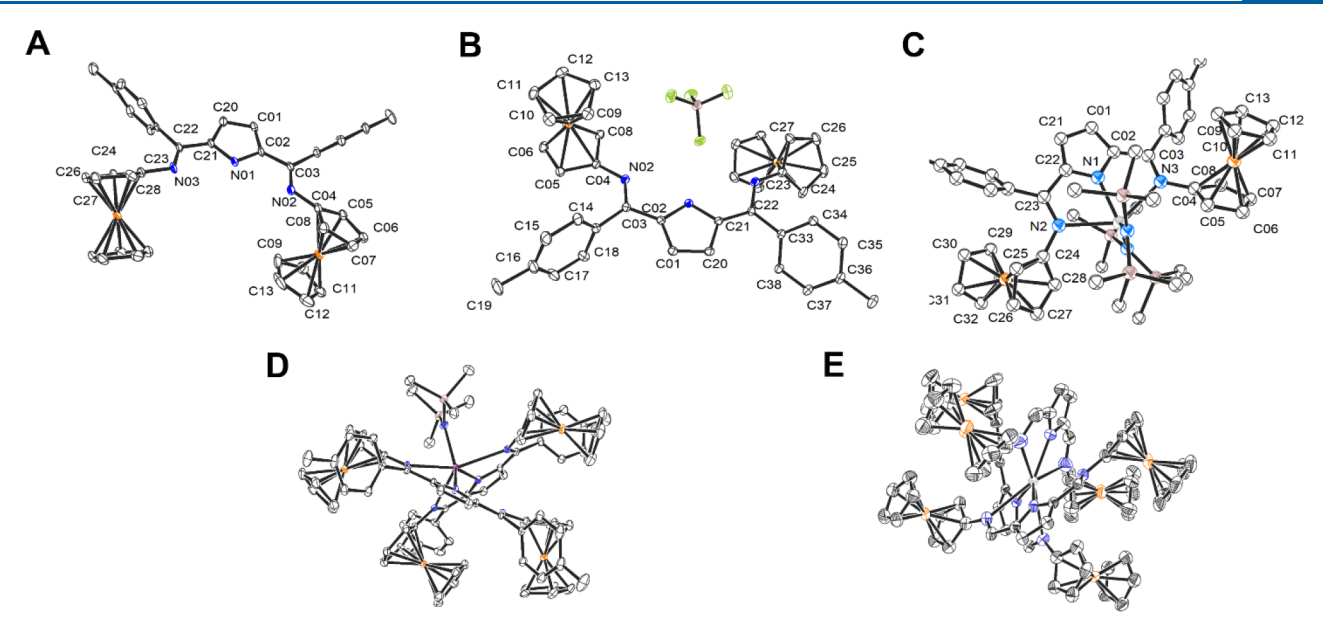
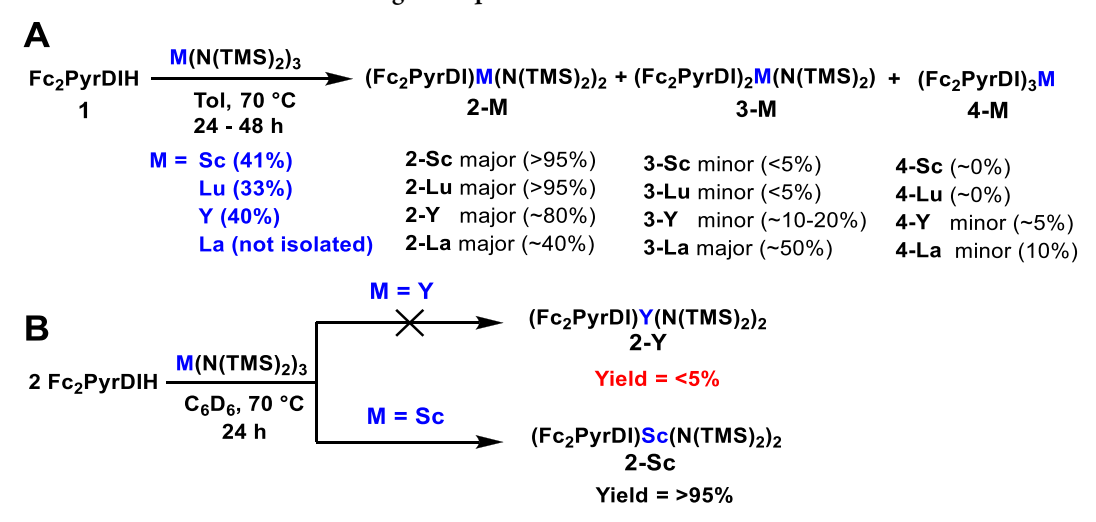


Figure 2. Crystal structures of (A)  $Fc_2PyrDIH$  (1), (B)  $[Fc_2PyrDIH]^{+[}BF_4]$  (1<sup>+</sup>), (C)  $(Fc_2PyrDI)_2Sc(N(TMS)_2)_2$  (2-Sc), (D)  $(Fc_2PyrDI)_2YN(TMS)_2$  (3-Y) (E)  $(Fc_2PyrDI)_3La$  (4-La). Ellipsoids are drawn at 50% probability, and hydrogen atoms are removed for clarity. For (E) p-tol groups are omitted, and only one molecule from the unit cell is shown to improve clarity. See Table 1 for the key bonding metrics of 1, 1<sup>+</sup>, and 2-Sc. CCDC deposition numbers for 1, 1<sup>+</sup>, 2-Sc, and 3-Y are 2217095, 2217096, 2217097, and 2218384, respectively. The data crystal for 4-La was not included in the CCDC database due to checkCIF errors, and the reasons are discussed in the SI (Page S22).

Scheme 2. (A) Yield Results of 1:1 Equiv Metalation Reactions of Ligand 1 with Various  $M(N(TMS)_2)_3$  Precursors. (B) Results of In Situ NMR Reactions with Two Ligand Equivalents to the Various 3-Metal Structures<sup>a</sup>



<sup>a</sup>Yields in blue are isolated yields, while others are NMR yields.

azeotropic acid removal. All reaction components are readily separated by chromatography on *deactivated* basic alumina (5–10% w/w  $\rm H_2O/Al_2O_3$  starting from Bockman I grade activated alumina) using a 15–40% EtOAc/hexanes gradient. Using activated alumina as received resulted in strong adsorption to the solid phase and poor separation, while silica chromatography resulted in rapid hydrolysis and/or protonation depending on the level of silica hydration. Protonation is readily identified by conversion to a green species. Red crystals of  $\rm Fc_2PyrDIH$  (1) can be obtained from layered water/THF, and the structure was verified by X-ray diffraction (Figure 2A). See below for additional 1 structural information.

As expected, the addition of 1 eq of AgBF<sub>4</sub> in THF to Fc<sub>2</sub>PyrDIH in DCM led to the formation of complex

[Fc<sub>2</sub>PyrDIH]<sup>+</sup>[BF<sub>4</sub>] (1<sup>+</sup>) (Scheme 1C, step b), which was also characterized by X-ray diffraction (Figure 2B).

**Metallation Reactions of 1.** Metallation of the  $Fc_2PyrDIH$  ligand was pursued via protodeamination of the appropriate  $M(N(TMS)_2)_3$  precursor with  $Fc_2PyrDIH$  (Scheme 2A). Trisamido metal precursors were employed because the bulky TMS groups apply steric pressure to prevent the free rotation of the ferrocene fragments (vide infra). Note that these complexes are significantly less air-stable than the parent trisamides, decomposing nearly instantly and stoichiometrically on exposure to trace air or moisture. Decomposition also occurred on storage inside the glovebox. Therefore, rigorously dry and deoxygenated solvents and reaction conditions are essential, and complexes were used immediately after synthesis. For these reasons, Teflon-sealed glass flasks

were used for metallation reactions and o-ring sealed glassware for workup and product isolation. Recycling of solvent for extraction, as described in the experimental, minimizes moisture introduction from trace levels in the solvent and facilitates purification. Thus, the addition of 1 equiv  $Fc_2PyrDIH$  (1) to  $Sc(N(TMS)_2)_3$  in toluene achieves quantitative formation (>95%, estimated by NMR yield) of 2-Sc after 48 h at 70 °C (Scheme 2A). The complex 2-Sc crystallizes as purple crystals from green solutions, and the structure was verified by X-ray diffraction (Figure 2C) and further characterized by NMR and UV/vis-NIR. For additional information about the structure of 2-Sc, see below. Similarly, the analogous Lu complex was obtained (2-Lu) in quantitative conversions using a 1:1 mixture of Fc<sub>2</sub>PyrDIH (1) and  $Lu(N(TMS)_2)_3$ . Complex 2-Lu can be isolated as a purple powder and was characterized by NMR and UV/vis-NIR, which supports the proposed structure. Attempts to grow single crystals suitable for X-ray measurement were unsuccessful due to partial decomposition during storage and during crystallization attempts, suggesting thermal instability.

While it was anticipated that the high steric congestion would inhibit multiple additions of 1 to  $M(N(TMS)_2)_3$  during metallation, at 1:1 stoichiometry, multiple addition prevails for the larger metal ions such as Y and La (Scheme 2A). For Y, this results in ~10-20% conversion to (Fc<sub>2</sub>PyrDI)<sub>2</sub>Y(N-(TMS)<sub>2</sub>) (3-Y) and nearly 50% conversion to the analogous La complex, 3-La. The addition of 2 equiv of 1 to Y(N(TMS)<sub>2</sub>)<sub>3</sub> affords no 2-Y at the end of the reaction, but the product displays the same <sup>1</sup>H NMR resonances as the impurities observed during 2-Y synthesis, implicating 3-Y as the likely source of the extra NMR resonances (Figure S12). The structure of 3-Y is also supported by X-ray diffraction (Figure 2D). Note that the same reaction using Sc(N-(TMS)<sub>2</sub>)<sub>3</sub> (Scheme 2B, Figure S10) does not result in multiple products, as judged by NMR, using either 1 or 2 equiv of 1. The formation of only 2-Sc suggests that the smaller  $Sc^{+3}$  size impedes the formation of 3-Sc. In the case of La, triple addition is also observed, yielding a 9-coordinate compound (4-La), (Fc<sub>2</sub>PyrDI)<sub>3</sub>La, (4-La). This species was challenging to observe via NMR due to broad features that overlap with multiple side products. However, it was characterized by X-ray diffraction (Figure 2E) during unsuccessful attempts to isolate 2-La. Observation by singlecrystal diffraction suggests that 4-La is a possible reaction product, indicating the consequence of the large La<sup>+3</sup> ionic radius on available metal-ligand stoichiometries, although not confirming it as a primary reaction product. Attempts to grow suitable X-ray crystals of 2-Y and 2-La were unsuccessful probably due to the presence of the over-addition products 3-Y, 3-La, and 4-La, which tend to crystallize first.

The low thermal stability of **2-Y** and **2-La**, which tend to decompose upon crystallization attempts, is another reason for the challenges in their isolation. The **2-M** complexes can be isolated in good purity by multiple heptane or pentane washes affording materials with fewer impurities based on NMR characterization. However, significant yield losses are observed, and the **3-M** complexes are still present in small quantities in **2-Y** samples (Figure S5). Note that selectivity for the monosubstituted **2-M** complexes can be enhanced by using stoichiometric excesses of  $M(N(TMS)_2)_3$  reagents, which suppresses multiple  $Fc_2PyrDIH$  additions. However, the excess lipophilic TMS groups in the reaction crude hindered isolation by crystallization or trituration. Attempts to sublime off the

excess metal precursor before pentane washing also led to diminished isolated yields despite improved product selectivity in the crude.

**Solid-State Structure Characterization.** Single crystals of Fc<sub>2</sub>PyrDIH (Figure 2A) grew spontaneously from column fractions (approximately 20% EtOAc/hexanes) during the course of chromatography. Single crystals of [Fc<sub>2</sub>PyrDIH]<sup>+</sup>[BF<sub>4</sub>] ([1]<sup>+</sup>) (Figure 2B) were grown by dissolving the crude product in toluene and layering with heptane. Over time, single crystals suitable for X-ray diffraction were obtained, although bulk isolable product was not obtained. 2-Sc was crystallized by slow evaporation of toluene into paratone oil using a vial-in-vial technique, with paratone oil in the outer vial (Figure 2C). Because 2-Y, 2-Lu, and 2-La undergo decomposition and/or rearrangement during crystallization, single crystal diffraction data could not be obtained, and instead, crystals of 3-Y and 4-La were obtained (Figure 2D,E).

The neutral Fc<sub>2</sub>PyrDI ligand 1 is planar within the pyrrolyl core, with slight torsions about the Cp rings. Ferrocene torsions were calculated by taking the dihedral angle between imine carbon, imine nitrogen, Cp  $\alpha$  carbon, and the Fe atom (e.g., C03, N2, C04, Fe1) and reporting the difference from 90° (deviation of the Fe-Cp axis being perpendicular to the pyrrole plane) (Figure 2). Neglecting differences in ferrocene torsion, 1, 2-Sc, and 3-Y are symmetric with respect to bonding metrics, and only one side of the Fc<sub>2</sub>PyrDI ligand is reported in Table 1. For 3-Y, "Fe1" and "Fe2" belong to the one Fc<sub>2</sub>PyrDI ligand, while "Fe3" and "Fe4" belong to the

Table 1. Key Bonding Metrics for the Indicated Structures in Figure 2  $(\mathring{A})$ 

| $Fc_2PyrDIH$ (1)                                          |                       |                    |          |
|-----------------------------------------------------------|-----------------------|--------------------|----------|
| Fc1 torsion                                               | 48.6(3)°              | Fc2 torsion        | 29.4(3)° |
| Fc1 Cp-Cp distance                                        | 3.314(2)              | Fc2 Cp-Cp distance | 3.290(2) |
| C03-N2                                                    | 1.291(4)              | C01-C21            | 1.413(4) |
| N1-C02                                                    | 1.374(3)              | C01-C02            | 1.389(5) |
| N2-C04                                                    | 1.403(4)              | C02-C03            | 1.456(4) |
| [Fc2PyrDIH][BF <sub>4</sub> ] ([1                         | l] <sup>+</sup> )     |                    |          |
| Fc1 torsion                                               | 29.75(8)°             | Fc2 torsion        | 6.11(8)° |
| Fc1 Cp-Cp distance                                        | 3.303(1)              | Fc2 Cp-Cp distance | 3.291(1) |
| C03-N2                                                    | 1.328(1)              | C01-C21            | 1.294(1) |
| N1-C02                                                    | 1.381(1)              | C01-C02            | 1.410(1) |
| N2-C04                                                    | 1.414(1)              | C02-C03            | 1.421(1) |
|                                                           |                       | C23-N3             | 1.294(1) |
| N1-C22                                                    | 1.356(1)              | C21-C22            | 1.400(1) |
| N3-C24                                                    | 1.395(1)              | C22-C23            | 1.455(1) |
| Fc <sub>2</sub> PyrDISc(N(TMS) <sub>2</sub> )             | ) <sub>2</sub> (2-Sc) |                    |          |
| Fc1 torsion                                               | 35.8(2)               | Fc2 torsion        | 38.4(2)  |
| Fc1 Cp-Cp distance                                        | 3.303(1)              | Fc2 Cp-Cp distance | 3.304(2) |
| C03-N2                                                    | 1.307(3)              | C01-C21            | 1.404(2) |
| N1-C02                                                    | 1.353(2)              | C01-C02            | 1.403(4) |
| N2-C04                                                    | 1.424(3)              | C02-C03            | 1.454(3) |
| (Fc <sub>2</sub> PyrDI) <sub>2</sub> YN(TMS) <sub>2</sub> | <sub>2</sub> (3-Y)    |                    |          |
| Fc1 torsion                                               | 35.4(5)               | Fc2 torsion        | 5.4(5)   |
| Fc1 Cp-Cp distance                                        | 3.310(3)              | Fc2 Cp-Cp distance | 3.283(3) |
| Fc3 torsion                                               | 11.3(5)               | Fc4 torsion        | 26.7(5)  |
| Fc3 Cp-Cp distance                                        | 3.308(3)              | Fc4 Cp-Cp distance | 3.296(3) |
| C03-N2                                                    | 1.308(5)              | C01-C21            | 1.385(6) |
| N1-C02                                                    | 1.357(5)              | C01-C02            | 1.410(5) |
| N2-C04                                                    | 1.423(5)              | C02-C03            | 1.446(6) |

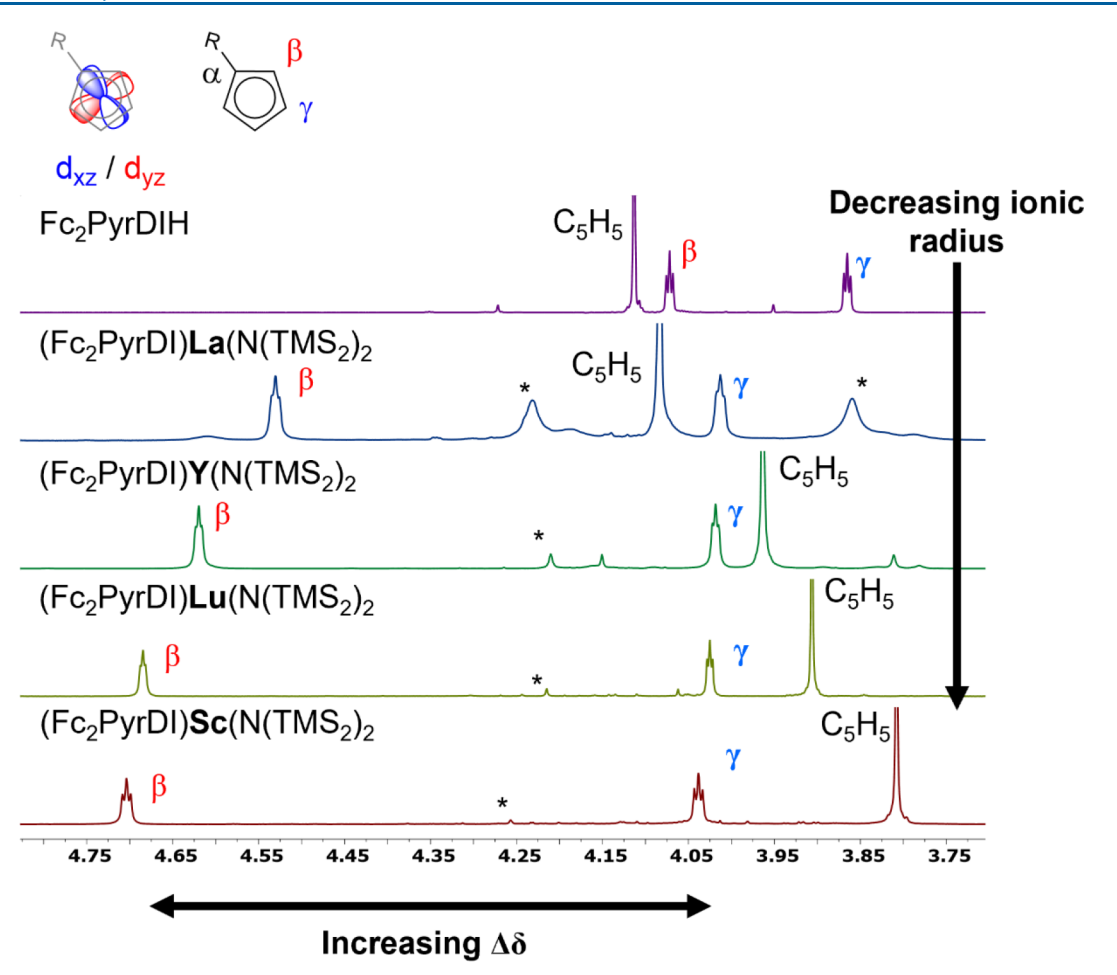


Figure 3. <sup>1</sup>H NMR spectra of the ferrocene protons for  $Fc_2PyrDI$  (1) and its metal complexes.  $\beta$  and  $\gamma$  assignments are based on homology with previously published pyridine analogs and confirmed by NOESY experiments. Stars indicate 3-M species.

other. The two Fc<sub>2</sub>PyrDI ligands on 3-Y show nearly identical bond metrics, so only one is reported in Table 1.

In contrast, the mixed valent species [1]<sup>+</sup> shows asymmetry in the bond lengths, and the ferrocenes adopt an *anti*-conformation. For [1]<sup>+</sup>, the region of the structure adjacent to the Fe(III) center exhibits bond elongation in the pyrrole ring (N1-C02) and imine (C03-N2), while the Fe(II) side shows bond contraction (N1-C22, and C23-N3) compared to the unoxidized ligand 1. The Cp-Cp distances (computed between the centroids of the Cp rings) are typical for ferrocene compounds and commensurate with oxidation to ferrocenium, as we observe an elongation of this distance.<sup>37-39</sup> We emphasize that oxidation state assignments are formal assignments based on a predominantly localized structure.

The Fe···Fe distance in ligand 1 is 8.834(3) Å, while the mixed valent species [1]\* has a 9.280(1) Å distance. For 2-Sc, this distance is 9.568(1) Å. For 3-Y, the two Fe···Fe distances (comparing two Fe atoms on the same Fc<sub>2</sub>PyrDI ligand) are 9.504(1) and 10.711(1). Attempts to grow single crystals of 2-Y, 2-Lu, and 2-La were unsuccessful. However, single crystals of 3-Y and 4-La were obtained in these crystallization attempts. While the solved structure for 4-La presented an unresolved alert in the IUCr checkCIF system, it gave sufficient diffraction to afford a good R factor (10.9% for 4-La) and unambiguously assigns the connectivity and stoichiometry as (Fc<sub>2</sub>PyrDI)<sub>3</sub>La (4-La). See the SI page S20 for discussion of the checkCIF alert.

NMR Spectroscopy. Because the pairs of ferrocene Cp protons on the functionalized ring are oriented differently along the ring, they experience different shielding effects by the  $d_{xz}/d_{yz}$  and  $d_{xy}/d_{x2}$ -<sub>y2</sub> orbitals (Figure 3). As such, electron donation and withdrawal effects of one orbital set versus the other will amplify magnetic nonequivalence. This difference in chemical shift,  $\Delta\delta$ , has been correlated with the electronwithdrawing/donating interaction with different d orbitals. 40-42 It should be noted that a monotonically increasing  $\Delta\delta$  trend is observed with Fc<sub>2</sub>PyrDIH metalation in the order of decreasing metal ionic radius, 2-La < 2-Y < 2-Lu < 2-Sc. This trend suggests that metalation with diamagnetic rare earth ions engenders a greater interaction between the Fc<sub>2</sub>PyrDI  $\pi$ system and the ferrocene d-orbitals and that the effect is larger when smaller metal ions are used. Such a d- $\pi$  interaction would produce a significant chemical shift difference compared to that when the d-orbitals do not interact.

Intriguingly, the substituted Cp protons become deshielded as the metal size decreases, but the unsubstituted ring becomes shielded. Differing interactions between the d orbitals and the organic  $\pi$ -system also affect CT properties, which is further discussed in UV/vis–NIR and DFT sections, where additional rare earth element ionic radius and electronic properties trends are identified. While we anticipate some influence on  $\Delta\delta$  from the different covalent bonding behaviors between Sc, Y, La, and Lu, the observed trend does not support the interpretation that the covalent bonding between pyrrole and rare earth ion

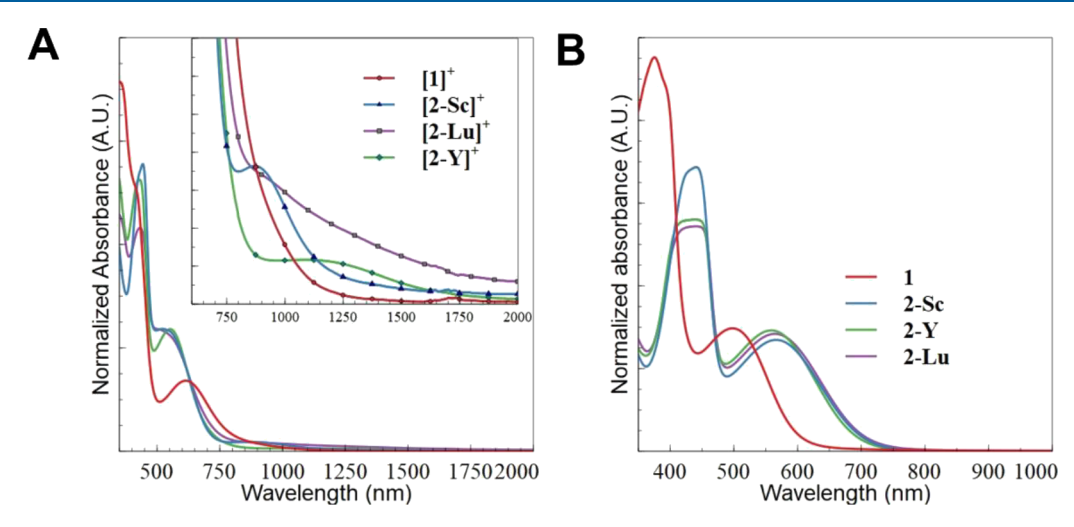


Figure 4. UV/visible-NIR spectra (normalized against total intensity) of  $Fc_2PyrDIH$  (1) and the  $(Fc_2PyrDI)M(N(TMS)_2)_2$  (2-M)complexes (M = Sc, Y, Lu), (A) before and after (B) addition of 1 equiv of oxidant (Magic Blue). Spectra were obtained on dimethoxyethane solutions.

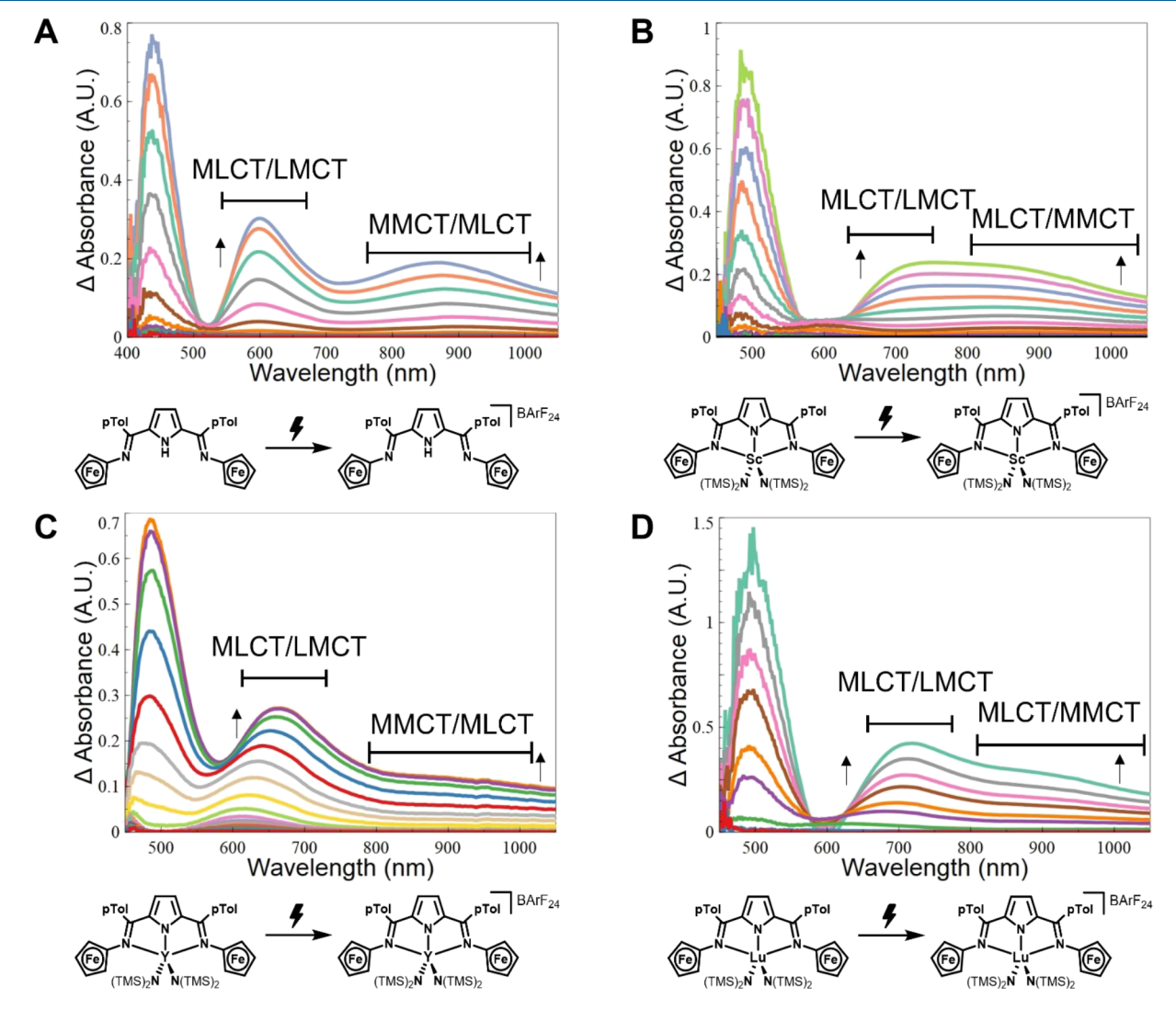


Figure 5. Spectroelectrochemistry plots of 1, 2-Sc, 2-Y, and 2-Lu solutions, represented in plots A, B, C, and D, respectively. Data were collected in dimethoxyethane with 100 Mm TBA-BarF $_{24}$  electrolyte, using a linear voltage sweep of 5 Mv/s. Scans were taken successively during electrolysis at  $\sim$ 25–50 Mv increments and plotted as difference spectra compared to the solution at 0 Mv. The difference spectra change with increasing voltage in the direction indicated by arrows. Colors are arbitrary to help distinguish different traces.

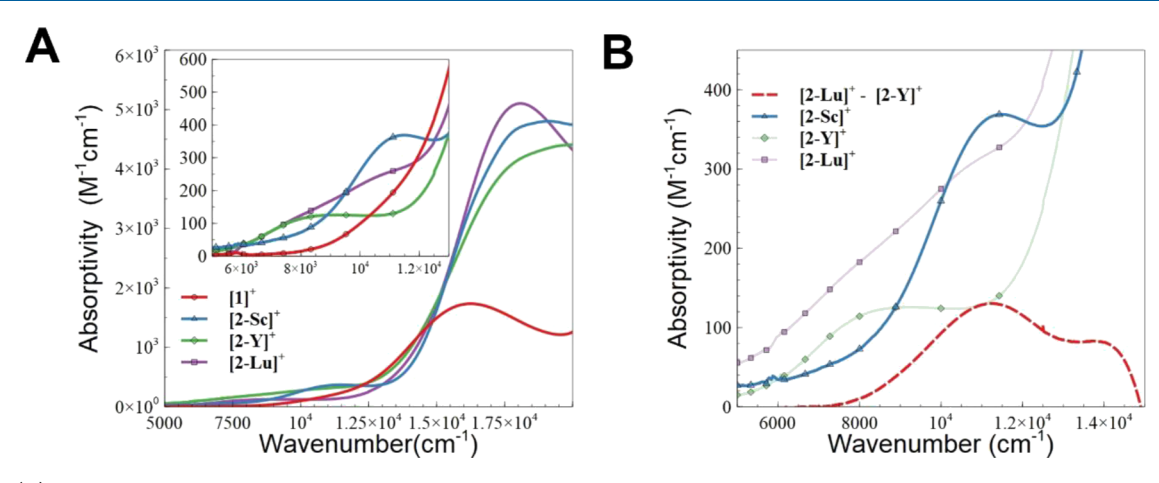


Figure 6. (A) Replot of the UV/vis-NIR data from Figure 4B in absorptivity and wavenumber units. Inset shows the NIR in detail. (B) Comparison of [2-Sc]<sup>+</sup> with the difference (red dashed) between the Y and Lu complexes (faded traces).

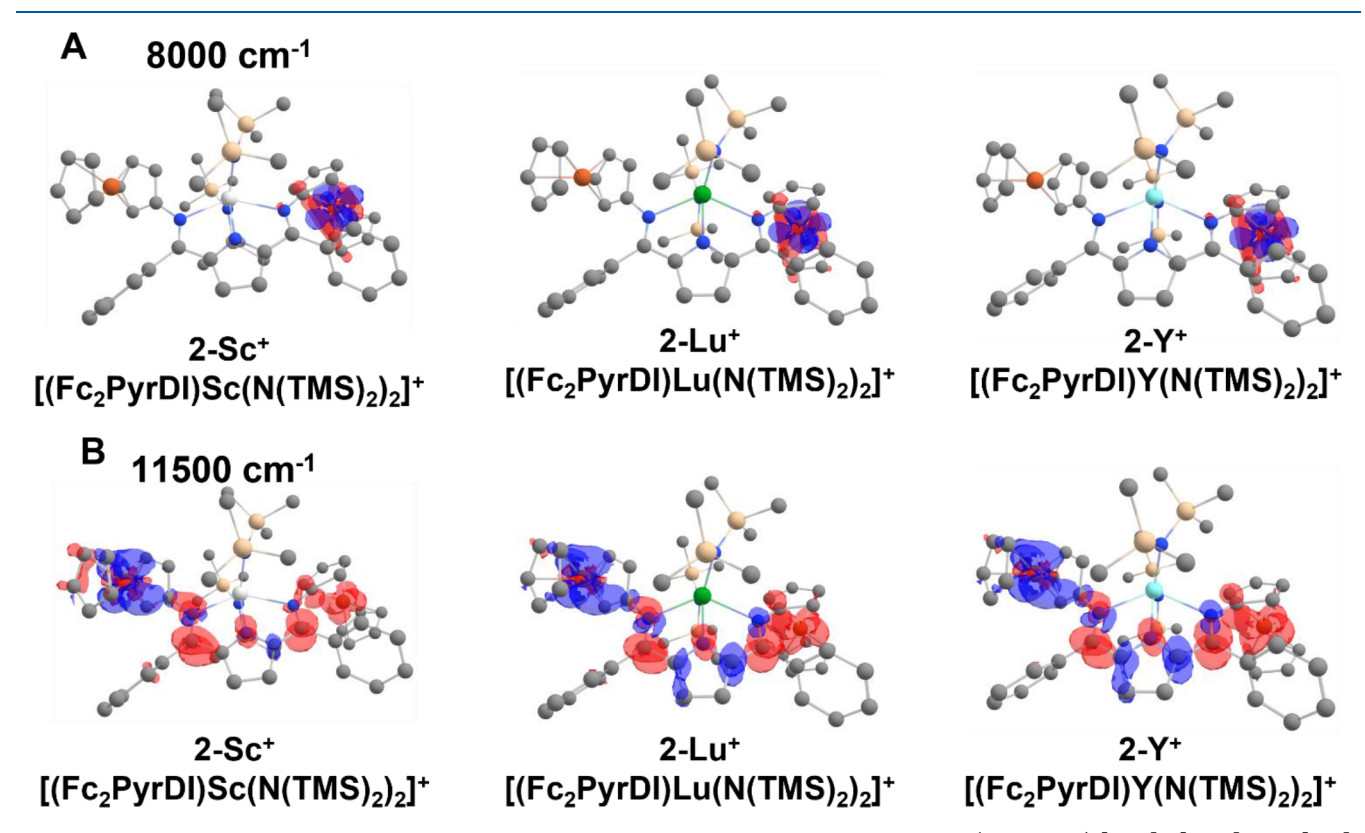


Figure 7. TDDFT computed difference density plots for the transitions that comprise the NIR bands for (left to right) [2-Sc]<sup>+</sup>, [2-Lu]<sup>+</sup>, and [2-Y]<sup>+</sup> for the features at (A) 8000 cm<sup>-1</sup> and (B) 11,500 cm<sup>-1</sup>. Blue represents electron density loss, while red represents electron density gain.

drives the changes in NMR shift. Nevertheless, scandium is notable for having more accessible d-orbitals and generally increased covalent behavior, exemplified by its ability to form imido and alkilidine compounds,  $^{43-45}$  which is unusual for the more ionic lanthanides. There is a predicted  $\pi$  interaction between the pyrrole nitrogen and scandium in the 2-Sc LUMO, for example (Figure S16). Similar to the  $\Delta\delta$  observed for ferrocenyl Cp protons, the p-tolyl protons also exhibit systematic shifts with rare earth ion identity, increasing in the same order as in the Cp spectra: La < Y < Lu < Sc. The ortho tolyl proton exhibits greatest shifts, presumably due to effects on the pyrrolyl  $\pi$ -system and closer proximity to the rare earth ion. Some shifts are seen in the pyrrolyl protons, but are of much smaller magnitude—despite being of similar distance to

the rare earth ion as the ortho tolyl protons. Increased effects for ortho tolyl protons suggests a contribution from changes in the pyrrolyl  $\pi$ -system (since the tolyl protons are structurally above the  $\pi$ -system, whereas the pyrrolyl protons are orthogonal to it).

**UV–Visible–NIR Optical Spectroscopy.** Due to the conjugation of the ferrocene with the diimino pyrrole  $\pi$ -system, the ferrocene d–d transition takes on charge transfer character and increases in intensity, redshifts, and broadens versus an isolated ferrocene. This is illustrated in a shift from 418 nm in free ferrocene 46 to 497 nm in 1 (Figure 4A). All the present 2-M complexes show a further redshift of this feature to ~560 nm (558, 564, and 566 nm for 2-Y, 2-Lu, and 2-Sc, respectively). If 1 equiv of the oxidant "Magic Blue" ([*p*Br-

Ph)<sub>3</sub>N][SbCl<sub>6</sub>]) is added to form [2-M]<sup>+</sup> species *in situ*, several new features appear between 550–2000 nm (Figure 4B) in all species, yielding a broadened and asymmetric band in the visible region and a new feature in the NIR. These features in the visible region are more clearly observed and analyzed via difference spectra (Figure 5 in the Spectroelectrochemistry section). The NIR regions for [2-Sc]<sup>+</sup>, [2-Y]<sup>+</sup>, and [2-Lu]<sup>+</sup> (800–2000 nm) show low-intensity broad features, which differ significantly depending on the metal identity.

The NIR features are best viewed in Figure 6A, plotting the absorptivity versus wavenumbers since the wavelength is not linear with respect to energy and thus distorts band shapes across this large range. Here, we see that the 2-Sc complex has higher energy and a narrower feature near 11,500 cm<sup>-1</sup>, while 2-Y shows lower energy and broader feature close to 8000 cm<sup>-1</sup>. **2-Lu**, however, appears to share characteristics of both. As evidenced by inspecting the difference spectrum of 2-Lu and 2-Y, which strongly resembles the 2-Sc NIR feature at 11,500 cm<sup>-1</sup> (Figure 6B), we suggest that [2-Sc]<sup>+</sup>, [2-Lu]<sup>+</sup>, and [2-Y]+ share similar transitions but in different weights. TDDFT analysis (vide infra) assigns the feature at 8000 cm<sup>-1</sup> as an interconfigurational d-d transition, while the feature at 11,500 cm<sup>-1</sup> shows a mixture of MMCT and MLCT characters ("Metal to Mixed Metal-Ligand Charge Transfer", MMMLCT; Figure 7). Regrettably, these species are not compatible with a useful range of solvents with which to perform a solvochromatic analysis.

**Spectroelectrochemistry.** The visible spectrum of the free Fc<sub>2</sub>PyrDI ligand displays a charge transfer excitation from ferrocene at 498 nm (Figure 5A). For [Fc<sub>2</sub>PyrDI]<sup>+</sup>, low energy features are observed between 550 and 1000 nm. Regarding the asymmetry of the main features centered at 600 and 900 nm, we suggest that there are overlapping transitions between 500-700 nm transitions that are a mixture of MLCTs from ferrocene to the pyrrole core and LMCTs to Fe(III).46 Congruency between spectra obtained by spectroelectrochemistry and chemical oxidation with Magic Blue supports production of the expected mixed valent species. For 2-Sc, 2-Lu, and 2-Y, we observe similar behavior to 1, but with features shifted to lower energies (Figures 6B-D). While more challenging to observe in the chemical oxidation experiments, the SEC difference spectra clearly show that all 2-M compounds have a common set of features around 900 nm but in different relative intensities and breadths. It should be noted that the relative intensity of the 900 nm feature decreases with  $[2-Sc]^+ > [2-Lu]^+ > [2-Y]^+ \sim [1]^+$ , congruent with observations from chemical oxidation (Figure 6A).

Because conventional electrochemistry solvents such as MeCN, DCM, and THF are reactive toward complexes 2-M under electrochemical conditions, dimethoxyethane was employed since it has dielectric constant and dipole moment similar to THF but does not undergo ring-opening polymerization. Attempts at collection of CV data for compounds 2-M led to unsatisfactory results that precluded analysis. Broad and irreversible waves are observed, presumably due to decomposition, and do not provide useful information. Consequently, we focus on the more informative optical data. Representative data for cyclic voltammetry can be found in the Supporting Information (Figures \$19-20). It should be noted that the agreement between optical data from a linear forward sweep in the SEC (Figure 5) and chemical oxidation (Figures 4 and 6) illustrates the suitability of this technique and analysis.

Compound 1 was suitable for traditional CV, however, and is presented in Figure 8. Conventional cyclic voltammetry was

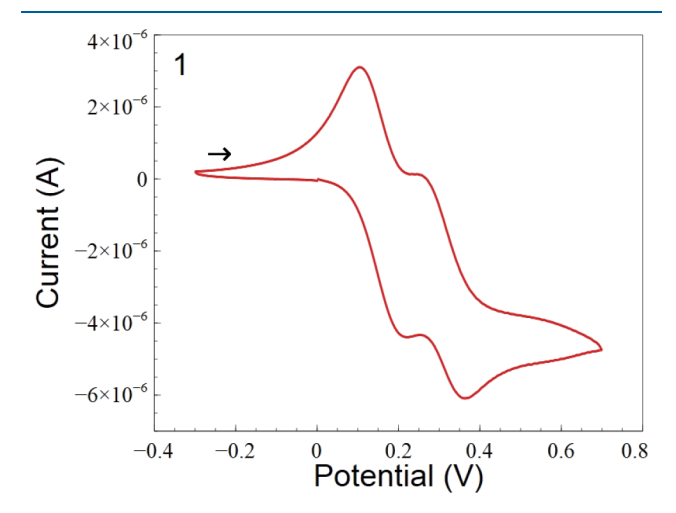


Figure 8. Cyclic voltammogram of  $Fc_2PyrDIH$  (1) taken in DCM with 100 mMol TBA-BArF, using platinum working and counter electrodes, with a silver wire pseudo reference.

performed in DCM with 100 mM TBA-BArF using platinum electrodes. From Figure 8, we observe a split between the two ferrocene oxidations, which was not observed in the previously studied pyridine analog. <sup>11</sup> This further supports the SEC data that show NIR charge transfer features, suggesting some degree of electronic coupling between ferrocenes in the free ligand. This coupling is further modified by the identity of the coordinated metal ion, rather than "switching" observed in the previously reported pyridine system. <sup>11</sup> The splitting between oxidation waves is 140 mV, as shown in Figure 8.

Theoretical Analysis. The computed bond lengths and angles for 1 are in good agreement with the experiment, with the exception that the DFT-optimized structure has minor, not unexpected, differences in ferrocene torsions (Table 3). Table S3 shows that computed optical spectra are in good agreement with the experiment, except for 1, where additional low energy transitions are predicted, which lead to the effective band position shifting to lower energy (535 vs 497 nm). This likely reflects the low energy barrier of ferrocene rotation, leading to single-point calculations deviating from experimental solutionstate behavior. The [Fc<sub>2</sub>PyrDI]<sup>+</sup> cation and (Fc<sub>2</sub>PyrDI)Sc(N-(TMS)<sub>2</sub>)<sub>2</sub> structures were optimized from the experimental crystal structures, with the removal of the BF<sub>4</sub> counterion from the [Fc<sub>2</sub>PyrDIH]<sup>+</sup>[BF<sub>4</sub>] crystal. The pyrrole metrical parameters for the computed 1<sup>+</sup> structure are in good agreement with crystal data despite the omission of the counterion (Table 3).

While the computed **2-M** structures are qualitatively similar throughout the series, certain bond angles and lengths show a trend with metal ionic radius. Notable elongation of the M- $N_{pyrrole}$  and M- $N(TMS)_2$  distances is observed with increasing metal ionic radius, while the ferrocene torsions within the same molecule become more dissimilar with increasing ionic radius ( $\Delta$ Fc-torsion = difference between Fc1 torsion and Fc2 torsion). Previously, in less encumbered pyridyl complexes and in the free Fc<sub>2</sub>PyrDIH ligand, oxidation causes the ferrocenes to distort and rotate out of the plane of the heterocyclic core (Figure 7). However, the geometries of [2-Sc]<sup>+</sup>, [2-Lu]<sup>+</sup>, and [2-Y]<sup>+</sup> limit this rotation, as the *p*Tol and  $N(TMS)_2$  groups restrict ferrocene group rotation. This rigidification is likely

one source of the difference in charge transfer properties between 1+ and [2-M]+ and further explains the differences between [2-Sc]+, [2-Lu]+, and [2-Y]+ (Table 3) as the ferrocene torsions are more similar in [2-Sc]+ compared to [2-Lu]+ and [2-Y]+ since the range of stable torsion angles is likely smaller in the more sterically congested complexes (Table 3 column 8: "ΔFc-torsion"). For consistency of comparison, "Fc1" denotes the ferrocene that undergoes oxidation in all entries shown in Table 3. A shorter M-N<sub>pyrrole</sub> distance and shorter M-N(TMS)<sub>2</sub> distances bring the bulky N(TMS)<sub>2</sub> groups closer to the ferrocenes and limit their rotational freedom, thereby restricting geometric changes on oxidation. This situation is also reflected in smaller changes in imine bond lengths on oxidation of 2-Sc to [2-Sc]<sup>+</sup>, correlating with the enforced symmetry between the ferrocene torsions. The differences in imine bond lengths in the mixed valent forms ( $\Delta C$ =N, Table 3 column 3) are 0.017, 0.029, and 0.030 Å for [2-Sc]<sup>+</sup>, [2-Lu]<sup>+</sup>, and [2-Y]<sup>+</sup>, respectively. The degree to which a mixed valent compound must rearrange is an important parameter in optical electron transfer, and the larger rare earth metal ions appear to allow greater structural asymmetry between the Fe(II) and Fe(III) halves of the mixed valent complex—evident in both the torsions and the imine bond lengths.

The computed visible spectra of the present neutral and mixed valent complexes are in good agreement with the experiment (Table S3). The frontier orbitals are qualitatively the same across the series of neutral compounds (1 and 2-M, Figure S16), except that in the LUMO, and there is a predicted  $\pi$ -interaction between Sc and the pyrrole nitrogen for 2-Sc, while this interaction is essentially nonexistent in 2-Y and 2-Lu. However, as seen in Figure 7B, little electron density is transferred to scandium in the 11,500 cm<sup>-1</sup> charge transfer although the LUMO is mixed into the transition in significant weight, the net contribution from scandium is small. This may help explain why metal ionic radius effects dominate over covalency effects as the rare earth ion participates comparatively little in the charge transfer. In the Marcus-Hush Classical 2-state formalism of evaluating MMCT bands, the excited state represents a direct metal-to-metal electron transfer. 1,47 Orbitals on the bridging ligand are thus not directly important in analyzing or interpreting the experimental charge transfer between metals in a two-state model. However, the superexchange formalism introduced by Brunschwig, Creutz, and Sutin 1,2 incorporates additional charge transfer states involving the bridging ligand in the model. Adding these CT states provides a three-state model for analyzing complex species where orbitals from the bridging ligand are important in facilitating the electron transfer. Inspection of the change in electron density during the NIR transitions for [2-M]<sup>+</sup> complexes reveals both MMCT and MLCT character, i.e., the donor orbital is largely centered on Fe-A, and the acceptor orbital has contribution from both the bridging ligand and Fe-B. From these plots, we see that pure MMCT is not operative, as there is also strong MLCT character as well. It is known that the HOMO-LUMO gap influences superexchange-mediated charge transfer, 48,49 and the charge density of the metal ion and thus its ionic radius for a series of 3<sup>+</sup> metal ions—may have an influence on the HOMO-LUMO gap, and consequently, the intensity of superexchange-mediated charge transfer between metals. Such an effect would rationalize the difference between 1<sup>+</sup> and [2-M]<sup>+</sup> NIR spectra, as well as the gradual CT intensity change with the ionic radius (Figure 4B).

Figure 7 shows difference density plots for the NIR transitions at 8000 and 11,500 cm<sup>-1</sup>. These plots reveal the difference in electron density between the ground and excited state for each transition. For all [2-M]<sup>+</sup> species, the 8000 cm<sup>-1</sup> feature represents a symmetry-forbidden d-d transfer, while at 11,500 cm<sup>-1</sup>, the transition takes on MMCT/MLCT mixed character. We note that as the torsion angle for the donor ferrocene ("Fc2-torsion", column 7 in Table 3) falls from [2- $Sc]^+ > [2-Lu]^+ > [2-Y]^+$ , the amount of pyrrole character in the donor orbitals increases, as seen in Figure 7, where the density loss is given by blue shading. While some uncertainties may exist for computed geometries for which we do not have crystallography to validate (in those cases, there is excellent agreement), the trends through the series of compounds are clearly evident. The DFT calculations may mostly reflect absolute error; however, relative errors between homologous compounds tend to be small. Therefore, we focus on comparing parameters between computed structures instead of investigating individual values—as comparative analysis is most reliable and informative.

#### DISCUSSION

While adaptations of Marcus theory have been successfully employed to describe electron transfer and electronic structures in various mixed valent systems, its generalizability to systems that are not predominantly valence localized or delocalized remains challenging.<sup>2,3</sup> This is in part because Marcus theory models the wavefunctions involved as metalcentered. This assumption becomes less straightforward when the orbitals involved in the electron transfer have contributions from the bridging ligand. 50,51 Models that include the bridging ligand then describe three different coupling parameters: HAL H<sub>BL</sub>, and H<sub>AB</sub>, which describe the coupling between metal A and the bridging ligand L, between metal B and the bridging ligand, and the direct coupling between metals A and B. It should be noted that for symmetric compounds,  $H_{AL} = H_{BL}$ . Efforts to refine these models include additional electronic states and vibrational couplings to better describe low energy transitions in systems as simple as biferrocene and applied to systems as complex as enzyme active sites. 2,52 In this scheme,  $H_{AB}$  may be small, but  $H_{AL}$  and/or  $H_{BL}$  may be significant and lead to charge transfer between metals via an intermediate state. In such cases, when the electronics and geometry of the bridging ligand are mechanistically Involved in electron transfer, greater attention must be paid to the influence of subtle structural factors from the bridging ligand.

While the different covalent bonding behaviors of Sc, Y, and Lu<sup>53</sup> might be expected to influence the  $\pi$  system and thus the optical properties arising from complexes with Fc<sub>2</sub>PyrDI, the spectra of 2-Sc, 2-Y, and 2-Lu are nearly identical. There is, however, a slight redshift across the series that correlates with the metal size (Figure 4A: band energy increases 8 nm across Sc < Lu < Y). This echos observations in the NMR shifts observed for the Cp protons, where the difference in chemical shift  $(\Delta \delta)$  between  $\beta$  and  $\gamma$  cp protons (Figure 3 and Table 2) decreases with increasing size. However, upon oxidation to their mixed valent forms, more marked differences are evident in the NIR for the  $[2-M]^+$  complexes.  $[2-Sc]^+$  shows a more intense, higher energy, narrower NIR feature, while [2-Y]+ displays weaker, lower energy, and broader feature. [2-Lu]+, however, appears to show an admixture of the two features. Thus, there do not appear to be significant differences in the optical features when the 2-M complexes are in the neutral

Table 2. <sup>1</sup>H Chemical Shifts for Cp Protons (ppm)

|                | 1    | 2-La | 2-Y  | 2-Lu | 2-Sc |
|----------------|------|------|------|------|------|
| Cp             | 4.11 | 4.08 | 3.96 | 3.91 | 4.81 |
| Ср-у           | 3.86 | 4.01 | 4.02 | 4.03 | 4.04 |
| Ср- <i>β</i>   | 4.06 | 4.53 | 4.62 | 4.68 | 4.71 |
| $\Delta\delta$ | 0.20 | 0.52 | 0.60 | 0.65 | 0.67 |

state where both Fe centers act as electron donors and neither is an acceptor. However, oxidation engenders significant differences between them when the two Fe centers make a donor—acceptor pair.

One possible origin of the above behavior is that in Class 1 and Class 2 mixed valent compounds, the metal centers have different coordination environments (bond lengths and bond angles between metal and ligands, etc.) due to the different oxidation states. Immediately after electron transfer, the structure must reorganize to accommodate the new coordination preferences of the new oxidation states at each metal center. In the highly congested [2-M]<sup>+</sup> complexes, these bonding reorganizations may be guided by steric factors. We have observed crystallographically that on oxidation, the Fe(III) center of 1<sup>+</sup> prefers to rotate out of the plane of the bridging ligand  $\pi$ -system to create torsion relative to the ferrocene Cp ring and the connected imine (Figure 2B). For all 2-M complexes, there is no significant change in the ferrocene torsion angle upon conversion to the mixed valent form (Table 3), which is a significant contrast to  $1/1^+$  and pyridyl analogs (Figure 1C). Within the  $2-M/[2-M]^+$  series, the ionic radius of the rare earth metal ion alters the size of the coordination sphere and, thus, the N(TMS)<sub>2</sub>—ferrocene group distance. With the bulky N(TMS)<sub>2</sub> ligands further from the ferrocenes, there is less steric pressure, allowing the ferrocenes to sample different rotations with respect to the imines, evident in the small torsion angle changes in 2-Sc/[2-Sc]+ versus 2-Lu/[2- $[Lu]^+$  and  $[2-Y]^+$ . Thus, when small geometric differences are fixed and not allowed to average over other conformation, such small changes can significantly influence mixed valent properties. For a series of ansa-biferrocenes, Dong et al. found that small differences in the tilt angle (the angle from which the Cp rings deviate from being parallel) of only 4.2° between ferrocene Cp rings change the coalescence temperature on the

Mössbauer timescale ( $\sim 10^{-7}$  s) from 365 K to 265 K. Also, the tilt angle lowered the HOMO–LUMO gap by nearly 0.5 eV.<sup>54</sup>

The above observations and TDDFT calculations also explain why the visible spectroscopic features for all compounds are similar, as they are dominated by transitions originating from predominantly ferrocene Fe d-orbitals and are accepted by orbitals that are largely pyrrolate centered (Figure 7). In contrast, the NIR transitions have a more mixed Fepyrrolate character in the excited state (Figure 7). Transitions with greater iron-pyrrolate delocalized character should be more influenced by ferrocene torsions, while those closer to typical MLCT would be expected to be less sensitive to the orbital overlaps between the ferrocene Fe and the pyrrolyl imine. TDDFT assigns the feature at ca. 8000 cm<sup>-1</sup> to a d-d transition while predicting the feature at 11,500 cm<sup>-1</sup> as having an MMCT character. For [2-Sc]<sup>+</sup>, the 8000 cm<sup>-1</sup> feature is weak, and the charge transfer is predominantly at 11,500 cm<sup>-1</sup>. However, this is inversely true for [2-Y]+, which only shows significant intensity at 8000 cm<sup>-1</sup>, while [2-Lu]<sup>+</sup> exhibits significant intensity for both. This validates the hypothesis that the rare earth coordination sphere size drives the different optical properties, as the ferrocene torsion angles decrease with the increasing metal ion size.

Applying the classical two-state Marcus-Hush analysis 1,2,47 yields a coupling constant,  $H_{AB}$ , of 264 cm<sup>-1</sup> and  $\Gamma$  = 0.2 for [2-Sc]<sup>+</sup>, while  $H_{AB}$  and  $\Gamma$  ~ 0 for [2-Y]<sup>+</sup> (the CT band at 11,500 cm<sup>-1</sup> is unresolved). We omit the [2-Lu]<sup>+</sup> analysis given the strong band overlap, but the band shape is similar to [2-Sc] but is lower intensity and broader (leading to intermediate  $H_{ab}$  and  $\Gamma$  values). Here,  $\Gamma$  represents a delocalization parameter and is given by  $\Gamma=1-\frac{\Delta\nu_{1/2}}{\Delta\nu_{0/2}^{\circ}}$ . This parameter describes how well the experimental band shape  $(\Delta \nu_{1/2})$  matches the band shape predicted by the Marcus—Hush theory, where  $\Delta \nu_{1/2}^{\circ} = \sqrt{16 \text{ln}(2) RT \nu_{\text{max}}}$ , and at room temperature, this becomes  $\Delta\nu_{1/2}^{\circ} = \sqrt{2310\nu_{\rm max}}$ . St Values of 0-0.1 describe strongly valence localized molecules and values of 0.2-0.5 describe weakly valence delocalized molecules. Values of 0.5-1 describe strongly delocalized systems approaching class III behavior. While a classical twostate model with direct MMCT is likely not mechanistically applicable in the present system, as evidenced by the difference

Table 3. Key Computed Bond Lengths and Torsions for 1, 1<sup>+</sup>, 2-M, and [2-M]<sup>+</sup> Complexes (Å)

|                     | $M-N_{pyrrole}$ | $C=N_{imine}$ | $\Delta C = N_{imine}$ | $M-N(TMS)_2$ | Fc1-torsion | Fc2-torsion | $\Delta$ Fc-torsion |
|---------------------|-----------------|---------------|------------------------|--------------|-------------|-------------|---------------------|
| 1                   | N/A             | 1.292         | 0.001                  | N/A          | 31.35°      | 14.92°      | 16.43°              |
|                     |                 | 1.291         |                        |              |             |             |                     |
| 1+                  | N/A             | 1.319         | 0.027                  | N/A          | 27.30°      | 2.34°       | 24.95°              |
|                     |                 | 1.292         |                        |              |             |             |                     |
| 2-Sc                | 2.112           | 1.306         | 0.000                  | 2.069        | 39.13°      | 39.45°      | $0.32^{\circ}$      |
|                     |                 | 1.306         |                        | 2.074        |             |             |                     |
| [2-Sc] <sup>+</sup> | 2.123           | 1.321         | 0.017                  | 2.055        | 38.31°      | 37.84°      | 0.47°               |
|                     |                 | 1.304         |                        | 2.063        |             |             |                     |
| 2-Lu                | 2.219           | 1.307         | 0.002                  | 2.191        | 38.04°      | 34.45°      | $3.59^{\circ}$      |
|                     |                 | 1.309         |                        | 2.192        |             |             |                     |
| [2-Lu] <sup>+</sup> | 2.228           | 1.333         | 0.029                  | 2.190        | 29.44°      | 35.89°      | 6.45°               |
|                     |                 | 1.304         |                        | 2.178        |             |             |                     |
| 2-Y                 | 2.274           | 1.307         | 0.002                  | 2.236        | 35.17°      | 25.41°      | 9.76°               |
|                     |                 | 1.309         |                        | 2.239        |             |             |                     |
| [2-Y] <sup>+</sup>  | 2.286           | 1.333         | 0.030                  | 2.220        | 27.82°      | 34.47°      | 6.65°               |
|                     |                 | 1.303         |                        | 2.232        |             |             |                     |
|                     |                 |               |                        |              |             |             |                     |

density plots showing significant pyrrolate character in these transitions (Figure 7), coupling parameters derived from 2 state models are typically in good agreement with three-state models for weakly coupled Class II systems.<sup>1</sup> It should be emphasized that for these transitions, the strong bridging ligand character renders the "MMCT" assignment imprecise since the charge transfer involves more than the two metal centers used in two-state models.<sup>2</sup> The energy and intensity are atypical of a general MMCT, affirming the TDDFT results that the amount of charge transfer between metals is less than that of pure MMCTs and falls between an MMCT and an MLCT.<sup>51,56</sup> This mixed character helps explain the low intensity and high energy of these features. We nevertheless computed apparent coupling constants and delocalization parameters for completeness and to compare these species.

#### CONCLUSIONS

When molecules experience large degrees of conformational freedom, it is difficult to deconvolute molecular and electronic structure effects due to solution averaging of different conformations. Here, we have restricted this conformational freedom to understand how minor structural changes caused by metal ionic radius variation influence mixed valent properties. In contrast to the previous study of pyridine trinuclear mixed valent systems (Figure 1A), 11 where we found that differing metal coordination chemistries have little effect on mixed valent properties; here, we have now focused instead on geometric factors. Previously, we found that metalation of the bis-ferrocenyl pyridinediimine ligand "switched" the system to a class II mixed valent molecule regardless of the metal identity. 11 However, in the present more congested and rigid Fc<sub>2</sub>PyrDI system, important differences in the optical charge transfer properties of [2-M]+ complexes depend on the rare earth ion radius employed, thereby increasing the coupling strength for smaller ions. By bringing ancillary N(TMS)<sub>2</sub> ligands closer to the ferrocenyl groups, the metal ion size influences the torsional angle between the Cp rings and attached imine, and consequently, the energy, band shape, and iron vs pyrrolate composition of their NIR charge transfers. We conclude that greater steric repulsion between N(TMS)<sub>2</sub> ligands and ferrocenes results in a more symmetric structure that lowers the reorganization energy and enhances the coupling between metal centers, as supported by the disappearance of a NIR charge transfer as the metal ion size increases and steric encumbrance is relieved. While [2-Sc]+ exhibits a dominant NIR feature at 11,500 cm<sup>-1</sup>, [2-Y]<sup>+</sup> displays one at 8000 cm<sup>-1</sup> and [2-Lu]<sup>+</sup> exhibits both features. Because MLCT states can be mixed with MMCT states, and in the Fc<sub>2</sub>PyrDI system, these MLCT states are significantly involved, the metal-ligand electronic coupling becomes an important parameter for the overall metal-metal coupling. The compounds in this study, 2-Sc, 2-Lu, and 2-Y do not engage in significant covalent bonding with the Fc<sub>2</sub>PyrDI ligand, but we find that the size of their coordination sphere limits the rotational freedom of the ferrocenyl groups. Using the two-state Marcus-Hush model, these bands correspond to a 264 cm<sup>-1</sup> coupling constant for [2-Sc]<sup>+</sup> and a negligible value for [2-Y]<sup>+</sup>. This observation gives substance to understanding structure relationships in mixed valent compounds as we demonstrated that multiple conformers must be considered to deconvolute spectra. Inspecting molecules to determine how static or fluxional the structure helps inform how strongly

intertwined geometry and electronics will be, guiding the design of new electronically coupled systems.

#### ASSOCIATED CONTENT

#### **Solution** Supporting Information

The Supporting Information is available free of charge at https://pubs.acs.org/doi/10.1021/acs.inorgchem.2c03973.

Crystal structures; DFT-optimized geometries; and NMR, calculated UV-vis, and representative electrochemical data for these complexes (PDF)

Results of 1 calculated (XYZ)

Results of 1<sup>+</sup> calculated (XYZ)

Results of 2-Lu calculated (XYZ)

Results of [2-Lu]<sup>+</sup> calculated (XYZ)

Results of 2-Sc calculated (XYZ)

Results of [2-Sc]<sup>+</sup> calculated (XYZ)

Results of 2-Y calculated (XYZ)

Results of [2-Y]+ calculated (XYZ)

#### **Accession Codes**

CCDC 2217095–2217097 and 2218384 contain the supplementary crystallographic data for this paper. These data can be obtained free of charge via www.ccdc.cam.ac.uk/data\_request/cif, or by emailing data\_request@ccdc.cam.ac.uk, or by contacting The Cambridge Crystallographic Data Centre, 12 Union Road, Cambridge CB2 1EZ, UK; fax: +44 1223 336033.

#### AUTHOR INFORMATION

#### **Corresponding Authors**

Yosi Kratish — Department of Chemistry, Northwestern University, Evanston, Illinois 60208-3113, United States; orcid.org/0000-0001-5279-0268; Email: yosi.kratish@northwestern.edu

Tobin J. Marks — Department of Chemistry, Northwestern University, Evanston, Illinois 60208-3113, United States; orcid.org/0000-0001-8771-0141; Email: t-marks@northwestern.edu

#### **Author**

Cole Carter – Department of Chemistry, Northwestern University, Evanston, Illinois 60208-3113, United States

Complete contact information is available at: https://pubs.acs.org/10.1021/acs.inorgchem.2c03973

#### Notes

The authors declare no competing financial interest.

#### ACKNOWLEDGMENTS

Financial support was provided by the National Science Foundation through the CHE-CAT program, Grant No. CHE-1856619 (C.C.). Financial support by the Office of Basic Energy Sciences, Department of Energy (DE-FG02-03ER15457) to the Institute for Catalysis in Energy Processes (ICEP) at Northwestern University (Y.K.) is gratefully acknowledged. This work used the IMSERC facility at Northwestern University, which has received support from the NSF (CHE-1048773 and CHE-9871268); Soft and Hybrid Nanotechnology Experimental (SHyNE) Resource (NSF NNCI-1542205); the State of Illinois and International Institute for Nanotechnology. In addition, this work made use of the GIANTFab core facility at Northwestern University. GIANTFab is supported by the Institute for Sustainability and Energy at Northwestern and the Office of the Vice President

for Research at Northwestern. We also thank Dr. N. La Porte for assistance in specEchem measurements, as well as Dr. Charlolette Stern for refining the crystal structure for **4-La** and **3-Y**.

#### REFERENCES

- (1) Brunschwig, B. S.; Sutin, N. Optical transitions of symmetrical mixed-valence systems in the Class II—III transition regime. *Chem. Soc. Rev.* **2002**, *31*, 168–184.
- (2) D'Alessandro, D. M.; Keene, R. Current Trends and Future Challenges in the Experimental, Theoretical and Computational Analysis of Intervalence Charge Transfer (IVCT) Transitions. *Chem. Soc. Rev.* **2006**, *35*, 424–440.
- (3) Demadis, K. D.; Hartshorn, C. M.; Meyer, T. J. The Localized-to-Delocalized Transition in Mixed-Valence Chemistry. *Chem. Rev.* **2001**, *101*, 2655–2686.
- (4) Stephen, B.; Dermot, O. H. Metal—Metal Interactions in Linked Metallocenes. *Chem. Rev.* **1997**, *97*, 637–670.
- (5) Kaim, W. Manifestations of Noninnocent Ligand Behavior. *Inorg. Chem.* **2011**, *50*, 9752–9765.
- (6) Kaim, W. The Shrinking World of Innocent Ligands: Conventional and Non-Conventional Redox-Active Ligands. *Eur. J. Inorg. Chem.* **2012**, 2012, 343–348.
- (7) Lyaskovskyy, V.; de Bruin, B. Redox Non-Innocent Ligands: Versatile New Tools to Control Catalytic Reactions. *ACS Catal.* **2012**, 2, 270–279.
- (8) Bart, S. C.; Chłopek, K.; Bill, E.; Bouwkamp, M. W.; Lobkovsky, E.; Neese, F.; Wieghardt, K.; Chirik, P. J. Electronic Structure of Bis(imino)pyridine Iron Dichloride, Monochloride, and Neutral Ligand Complexes: A Combined Structural, Spectroscopic, and Computational Study. *J. Am. Chem. Soc.* **2006**, *128*, 13901–13912.
- (9) Bouwkamp, M. W.; Bowman, A. C.; Lobkovsky, E.; Chirik, P. J. Iron-Catalyzed  $[2\pi + 2\pi]$  Cycloaddition of  $\alpha,\omega$ -Dienes: The Importance of Redox-Active Supporting Ligands. *J. Am. Chem. Soc.* **2006**, *128*, 13340–13341.
- (10) Chirik, P. J.; Wieghardt, K. Radical Ligands Confer Nobility on Base-Metal Catalysts. *Science* **2010**, 327, 794–795.
- (11) Carter, C.; Kratish, Y.; Jurca, T.; Gao, Y.; Marks, T. J. Bis-Ferrocenyl-Pyridinediimine Trinuclear Mixed-Valent Complexes with Metal-Binding Dependent Electronic Coupling: Synthesis, Structures, and Redox-Spectroscopic Characterization. *J. Am. Chem. Soc.* **2020**, 142, 18715–18729.
- (12) Connelly, N. G.; Damhus, T.; Hartshorn, R. M.; Hutton, A. T. Nomenclature of Inorganic Chemistry; RSC Publishing, 2005.
- (13) Aspinall, H. C. Chemistry of the f-Block Elements; Gordon and Breach Science Publishers, 2001.
- (14) Shannon, R. D. Revised effective ionic-radii and systematic studies of interatomic distances in halides and chalcogenides. *Acta Crystallogr., Sect. A* **1976**, *A32*, 751.
- (15) Martinez-Gomez, N. C.; Vu, H. N.; Skovran, E. Lanthanide Chemistry: From Coordination in Chemical Complexes Shaping Our Technology to Coordination in Enzymes Shaping Bacterial Metabolism. *Inorg. Chem.* **2016**, *55*, 10083–10089.
- (16) Kong, X. H.; Wu, Q. Y.; Lan, J. H.; Wang, C. Z.; Chai, Z. F.; Nie, C. M.; Shi, W. Q. Theoretical Insights into Preorganized Pyridylpyrazole-Based Ligands toward the Separation of Am(III)/Eu(III). *Inorg. Chem.* **2018**, *57*, 14810–14820.
- (17) Klamm, B. E.; Windorff, C. J.; Celis-Barros, C.; Marsh, M. L.; Meeker, D. S.; Albrecht-Schmitt, T. E. Experimental and Theoretical Comparison of Transition-Metal and Actinide Tetravalent Schiff Base Coordination Complexes. *Inorg. Chem.* **2018**, *57*, 15389–15398.
- (18) Borys, A. Schlenk Line Survival Guide. https://schlenklinesurvivalguide.com/ (accessed October 18, 2022).
- (19) McLlwrick, C. R. The removal of oxygen from gas streams: applications in catalysis and gas chromatography. *J. Phys. E: Sci. Instrum.* 1973, 6, 1208.

- (20) Roemer, M.; Nijhuis, C. A. Syntheses and Purification of the Versatile Synthons Iodoferrocene and 1,1'-Diiodoferrocene. *Dalton Trans.* **2014**, 43, 11815–11818.
- (21) Leonidova, A.; Joshi, T.; Nipkow, D.; Frei, A.; Penner, J.-E.; Konatschnig, S.; Patra, M.; Gasser, G. An Environmentally Benign and Cost-Effective Synthesis of Aminoferrocene and Aminoruthenocene. *Organometallics* **2013**, *32*, 2037–2040.
- (22) Bradley, D. C.; Ghotra, J. S.; Hart, F. A. Low co-ordination numbers in lanthanide and actinide compounds. Part I. The preparation and characterization of tris{bis(trimethylsilyl)-amido}-lanthanides. J. Chem. Soc., Dalton Trans. 1973, 10, 1021–1023.
- (23) McNeece, A. J.; Chang, M. C.; Filatov, A. S.; Anderson, J. S. Redox Activity, Ligand Protonation, and Variable Coordination Modes of Diimino-Pyrrole Complexes of Palladium. *Inorg. Chem.* **2018**, *57*, 7044–7050.
- (24) Neese, F. Software update: The ORCA program system—Version 5.0. Wiley Interdiscip. Rev.: Comput. Mol. Sci. 2022, 12, No. e1606.
- (25) Becke, A. D. Density-functional thermochemistry. III. The role of exact exchange. *J. Chem. Phys.* **1993**, *98*, 5648–5652.
- (26) Lee, C.; Yang, W.; Parr, R. G. Development of the Colle-Salvetti correlation-energy formula into a functional of the electron density. *Phys. Rev. B: Condens. Matter Mater. Phys.* **1988**, *37*, 785–789.
- (27) Vosko, S. H.; Wilk, L.; Nusair, M. Accurate spin-dependent electron liquid correlation energies for local spin density calculations: a critical analysis. *Can. J. Phys.* **1980**, *58*, 1200–1211.
- (28) Stephens, P. J.; Devlin, F. J.; Chabalowski, C. F.; Frisch, M. J. Ab Initio Calculation of Vibrational Absorption and Circular Dichroism Spectra Using Density Functional Force Fields. *J. Phys. Chem.* **1994**, 98, 11623–11627.
- (29) Scalmani, G.; Frisch, M. J. Continuous surface charge polarizable continuum models of solvation. I. General formalism. *J. Chem. Phys.* **2010**, *132*, 114110.
- (30) Wohlfarth, C. Static Dielectric Constants of Pure Liquids and Binary Liquid Mixtures (Supplement to IV/6); Springer Materials, 2008
- (31) Wohlfarth, C. Refractive Indices of Pure Liquids and Binary Liquid Mixtures (Supplement to III/38); Springer, 2008.
- (32) Dolomanov, O. V.; Blake, A. J.; Champness, N. R.; Schröder, M. OLEX: new software for visualization and analysis of extended crystal structures. *J. Appl. Crystallogr.* **2003**, *36*, 1283–1284.
- (33) Sheldrick, G. M. SHELXT Integrated Space-Group and Crystal-Structure Determination. *Acta Crystallogr., Sect. A: Found. Adv.* **2015**, *71*, 3–8.
- (34) Sheldrick, G. M. Crystal structure refinement with SHELXL. Acta Crystallogr., Sect. C: Struct. Chem. 2015, 71, 3-8.
- (35) Connelly, N. G.; Geiger, W. E. Chemical Redox Agents for Organometallic Chemistry. *Chem. Rev.* **1996**, *96*, 877–910.
- (36) Wright, A. C.; Du, Y. E.; Stoltz, B. M. Small-Scale Procedure for Acid-Catalyzed Ketal Formation. *J. Org. Chem.* **2019**, *84*, 11258–11260.
- (37) Hildebrandt, A.; Schaarschmidt, D.; Lang, H. Electronically Intercommunicating Iron Centers in Di- and Tetraferrocenyl Pyrroles. *Organometallics* **2011**, *30*, 556–563.
- (38) Hildebrandt, A.; Schaarschmidt, D.; Claus, R.; Lang, H. Influence of Electron Delocalization in Heterocyclic Core Systems on the Electrochemical Communication in 2,5-Di- and 2,3,4,5-Tetraferrocenyl Thiophenes, Furans, and Pyrroles. *Inorg. Chem.* **2011**, *50*, 10623–10632.
- (39) Frenzel, P.; Korb, M.; Hildebrandt, A.; Lang, H. Synthesis and Electrochemical Behavior of Ferrocenyl-Functionalized Metallocenes  $M(\eta^5-C_5H_5)_2(EFc)_2$  (M = Ti, Zr; E = O, S, Se). Eur. J. Inorg. Chem. **2018**, 2018, 3156–3163.
- (40) Sato, M.; Sekino, M.; Akabori, S. Pd(BF<sub>4</sub>)<sub>2</sub> Complexes of 1,1′-Bis[(alkyl- or aryl-)thio]-and 1,1′-Bis(diphenylphosphino)-Ferrocenes. Bond Formation Between the Fe and Pd Atoms. *J. Organomet. Chem.* **1988**, 344, C31–C34.
- (41) Stegner, P.; Farber, C.; Oetzel, J.; Siemeling, U.; Wiesinger, M.; Langer, J.; Pan, S.; Holzmann, N.; Frenking, G.; Albold, U.; Sarkar, B.;

**Inorganic Chemistry** Article pubs.acs.org/IC

- Harder, S. d-d Dative Bonding Between Iron and the Alkaline Earth Metals Calcium, Strontium and Barium. Angew. Chem., Int. Ed. 2020, 59, 2-14620.
- (42) Akabori, S.; Kumagai, T.; Shirahige, T.; Sato, S.; Kawazoe, K.; Tamura, C.; Sato, M. Preparation of Novel Platinum and Palladium Complexes by Reaction of 1,1'-Metallocenedichalcogenols with Tetrakis(triphenylphosphine)palladium(0) or -platinum(0). The Important Role of the Coordinating Ability of the Metal Atom of the Metallocene in Product Formation. Organometallics 1987, 6, 526-531.
- (43) Huang, W.; Khan, S. I.; Diaconescu, P. L. Scandium Arene Inverted-Sandwich Complexes Supported by a Ferrocene Diamide Ligand. J. Am. Chem. Soc. 2011, 133, 10410-10413.
- (44) Huang, W.; Carver, C. T.; Diaconescu, P. L. Transmetalation Reactions of a Scandium Complex Supported by a Ferrocene Diamide Ligand. Inorg. Chem. 2011, 50, 978-984.
- (45) Clough, B. A.; Mellino, S.; Clot, E.; Mountford, P. New Scandium Borylimido Chemistry: Synthesis, Bonding, and Reactivity. J. Am. Chem. Soc. 2017, 139, 11165-11183.
- (46) Sohn, Y. S.; Hendrickson, D. N.; Gray, H. B. Electronic Structure of Metallocenes. J. Am. Chem. Soc. 1971, 93, 3603-3612.
- (47) Brunschwig, B. S.; Sutin, N. Energy surfaces, reorganization energies, and coupling elements in electron transfer. Coord. Chem. Rev. 1999, 187, 233-254.
- (48) Giuffrida, G.; Campagna, S. Influence of Peripheral Ligands on the Metal-Metal Interaction in Dinuclear Metal Complexes with N-Heterocyclic Bridging Ligands. Coord. Chem. Rev. 1994, 135, 517-
- (49) Richardson, D. E.; Taube, H. Mixed-valence molecules: Electronic delocalization and stabilization. Coord. Chem. Rev. 1984, 60, 107-129.
- (50) Hayashi, M.; Takahashi, Y.; Yoshida, Y.; Sugimoto, K.; Kitagawa, H. Role of d-Elements in a Proton-Electron Coupling of  $d-\pi$  Hybridized Electron Systems. J. Am. Chem. Soc. 2019, 141,
- (51) Kubo, T.; Ohashi, M.; Miyazaki, K.; Ichimura, A.; Nakajima, K. Synthesis, Structure, and Cooperative Proton-Electron Transfer Reaction of Bis(5,6-diethylpyrazinedithiolato)metal Complexes (M = Ni, Pd, Pt). Inorg. Chem. 2004, 43, 7301-7307.
- (52) Warratz, R.; Tuczek, F. Low-Energy Bands of Ferrocene-Ferrocenium Dimers: Bandshape Analysis with a Four-Level Two-Mode Vibronic Coupling Configuration Interaction (VCCI) Model Including Asymmetry. Inorg. Chem. 2009, 48, 3591-3607.
- (53) Axe, J. D.; Burns, G. Influence of Covalency upon Rare-Earth Ligand Field Splittings. Phys. Rev. 1966, 152, 331-340.
- (54) Dong, T.-Y.; Lee, S.-H.; Chang, C.-K.; Lin, H.-M.; Lin, A. K.-J. Pronounced Effects of Ring Tilting on Rates of Intramolecular Electron Transfer in Polyalkyl-Substituted Mixed-Valence Biferrocenium Triiodides. Organometallics 1997, 16, 2773-2786.
- (55) Aguirre-Etcheverry, P.; O'Hare, D. Electronic communication through unsaturated hydrocarbon bridges in homobimetallic organometallic complexes. Chem. Rev. 2010, 110, 4839-4864.
- (56) Hayashi, M.; Takahashi, Y.; Yoshida, Y.; Sugimoto, K.; Kitigawa, H. Role of d-Elements in a Proton-Electron Coupling of  $d-\pi$  Hybridized Electron Systems. J. Am. Chem. Soc. 2019, 141, 11586-11693.

### **□** Recommended by ACS

### Structural and Magnetization Dynamics of Borohydride-**Bridged Rare-Earth Metallocenium Cations**

Christopher G. T. Price, Richard A. Layfield, et al.

ILINE 14 2023

INORGANIC CHEMISTRY

READ 2

#### **Chromium-Lanthanide Complexes Containing the** Cr=P=Cr Fragment: Synthesis, Characterization, and **Computational Study**

Mikhail Yu. Afonin, Sergey N. Konchenko, et al.

JUNE 22, 2023

INORGANIC CHEMISTRY

READ **C** 

#### Enabling Valence Delocalization in Iron(III) Macrocyclic **Complexes through Ring Unsaturation**

Reese A. Clendening, Tong Ren, et al.

JUNE 30, 2023

INORGANIC CHEMISTRY

RFAD 17

#### Iron(II) Complexes of 2,6-Di[4-(ethylcarboxy)pyrazol-1yl]pyridine with Reversible Guest-Modulated Spin-Crossover **Behavior**

Víctor García-López, Eugenio Coronado, et al.

MARCH 02, 2023

**CRYSTAL GROWTH & DESIGN** 

RFAD 🗹

Get More Suggestions >